Marine biogeochemical cycling and oceanic CO_2 uptake simulated by the NUIST Climate System Model: NUIST-CSM-2.0.1

Yifei Dai[1], Long Cao[2], Bin Wang[1, 3]

[1] Earth System Modeling Center, and Key Laboratory of Meteorological Disaster of Ministry of Education, Nanjing University of Information Science and Technology, Nanjing 210044, China
[2] Department of Atmospheric Sciences, School of Earth Sciences, Zhejiang University, Hangzhou 310027, China
[3] Department of Atmospheric Sciences and Atmosphere-Ocean Research Center, University of Hawaii, Honolulu HI 96822, USA

*Correspondence: longcao@zju.edu.cn

Abstract. In this study, we introduce and evaluate the performance of the Nanjing University of Information Science & Technology Climate System Model, version 2.0.1 (hereafter NUIST-CSM-2.0.1) that couples the atmosphere and ocean climate model with a marine biogeochemical component. Compared with available observations and data-based estimates, NUIST-CSM-2.0.1 reproduces reasonably well large-scale ocean carbon-related fields, including nutrients (phosphate, nitrate, and silicate), chlorophyll, and net primary production. However, some noticeable discrepancies between model simulations and observations are found in the deep ocean and coastal regions. Model-simulated current-day oceanic CO_2 uptake compares well with data-based estimates. From pre-industrial time to 2011, the modeled cumulative CO_2 uptake is 144 PgC, compared with data-based estimates of 155 ± 30 PgC. Diagnosed from the end of the 140-year benchmark 1% per year CO_2 increase simulations, the carbon-climate sensitivity parameter, which represents the sensitivity of integrated oceanic CO_2 uptake to CO_2-induced warming, is -7.1 PgC/K; The carbon-concentration sensitivity parameter, which represents the sensitivity of integrated oceanic CO_2 uptake to an increase in atmospheric CO_2, is 0.81 PgC/ppm. For comparison, carbon-climate and carbon-concentration sensitivity parameter diagnosed from CMIP5 (Coupled Model Intercomparison Project phase 5) model simulations under the same 1% per year CO_2 simulations range from -2.4 to -12.1 PgC/K (with a mean of -7.8 PgC/K) and 0.7 to 0.9 PgC/ppm (with a mean of 0.8 PgC/ppm), respectively. Our results demonstrate that the current version of NUIST-CSM-2.0.1 can be used as a useful tool to investigate the behavior of the ocean carbon cycle and its response to climate change under prescribed atmospheric CO_2 concentration scenarios.

1 Introduction

The global carbon cycle plays an important role in the climate system. The increase in atmospheric carbon dioxide (CO_2) is responsible for a large part of the observed increase in global mean surface temperature (Ciais et al., 2013). From 1750 to 2016, about 645±80 PgC (1 PgC =10^{15} gram carbon) of anthropogenic carbon has been emitted to the atmosphere, including 420±20 PgC from fossil fuels and industry and 225±75 PgC from land-use-change (Le Quéré et al., 2017). This CO_2 emission caused

atmospheric CO_2 concentration to increase by 45% from an annual mean pre-industrial value of ~277 parts per million (ppm) (Joos and Spahni, 2008) to 404 ppm in 2016 (NOAA ESRL Global Monitoring Division, 2016).

The ocean carbon cycle is one of the main components of the global carbon cycle. As a large carbon reservoir, the global ocean contains more than 50 times the amount of carbon than the atmosphere (Denman et al., 2007). The global ocean also plays a key role in anthropogenic CO_2 uptake (Ballantyne et al., 2012; Wanninkhof et al., 2013). From pre-industrial time to now, about 25% of anthropogenic CO_2 (about 160±20 PgC) has been absorbed by the ocean (Le Quéré et al., 2017). The ocean carbon cycle involves many complex physical, chemical, and biological processes such as chemical reaction of water molecules with dissolved CO_2, biological uptake of CO_2 through photosynthesis by phytoplankton in the upper ocean, and transport of inorganic and organic carbon into the ocean interior (solubility pump, soft tissue pump, and $CaCO_3$ pump) (Sarmiento and Gruber, 2006).

An increase in atmospheric CO_2, by perturbing the atmospheric radiation balance, leads to climate change. Changes in atmospheric temperature, precipitation, evaporation, and wind, induce changes in ocean physical properties such as temperature, salinity, and ocean circulation (Levitus et al., 2000; Gregory et al., 2005; Pierce et al., 2012). These changes in ocean physical properties, in turn, affect the ocean carbon cycle (Sarmiento and Gruber, 2006). Previous studies show that the global warming would reduce ocean's uptake of anthropogenic CO_2 (Cox et al., 2000; Zickfeld et al., 2008). For example, increasing sea surface temperature can directly decrease the CO_2 solubility and increase the oceanic pCO_2, and then result in the reduction of oceanic CO_2 uptake (Najjar 1992; Teng et al., 1996). Also, increasing temperature would decrease the buffer factor in the seawater (Yi et al., 2001). Changes in wind speed can also directly influence sea-air carbon exchange by changing gas transfer velocity (Wanninkhof 1992; Wanninkhof and Trinanes 2017). Meanwhile, global warming would also lead to a weakening of the global thermohaline circulation and an increase in ocean stratification (Gregory et al., 2005), which would not only reduce the transport of anthropogenic CO2 from the surface to deep ocean, but also reduce the upward transport of carbon and nutrient from the ocean interior. Global warming would also cause a shoaling of the mixed layer depth, increasing the average mixed-layer light, which would, in turn, affect phytoplankton growth and CO_2 uptake (Polovina et al., 2008; Luo et al., 2009; Steinacher et al., 2010; Capotondi et al., 2012). Therefore, it is important to gain a good understanding of the potential effect of global warming on the ocean carbon cycle.

Friedlingstein et al., (2006) proposed that the response of oceanic uptake of atmospheric CO_2 can be represented by the linear sum of two components: 1) carbon-concentration sensitivity, which refers to the response of oceanic CO_2 uptake to increasing atmospheric CO_2 alone; 2) carbon-climate sensitivity, which refers to the response of oceanic CO_2 uptake to CO_2-induced warming alone. Adopting the conceptual framework of Friedlingstein et al., (2006), a number of studies have analyzed the effect of CO_2 concentration and CO_2-induced warming on the carbon cycle in terms of the carbon-concentration and carbon-climate sensitivity parameters under different CO_2 emission and concentration scenarios (Gregory et al., 2009; Boer and Arora, 2009; Arora et al., 2013).

Given the importance of carbon cycle feedback in current and future global climate change, it is necessary to include the representation of the global carbon cycle in Earth system models (Bretherton, 1985; Menon et al., 2007). In 2014, a coupled

climate system model, Nanjing University of Information Science and Technology Climate System Model version 1.0 (NUIST-CSM v1.0), was developed, which consists of three main components, including European Centre Hamburg Atmospheric Model (ECHAM v5.3) (Roeckner et al., 2003), Nucleus for European Modeling of the Ocean version 3.4 (NEMO v3.4-revision 3814) (Madec and NEMO team, 2012) and Los Alamos sea-ice model version 4.1 (CICE v4.1) (Hunke and Lipsomb, 2010). NUIST-CSM v1.0 realistically reproduces large-scale present-day climatic fields such as sea surface temperature (SST) and precipitation, and large-scale climate variability and climate modes such as El Niño–Southern Oscillation (ENSO) and Madden–Julian oscillation (MJO) are also well reproduced (Cao et al., 2015). Recently, the new version of NUIST-CSM-2.0.1 was developed. In this new version, the *Pelagic Interactions Scheme for Carbon and Ecosystem Studies* (PISCES v2) is coupled to the ocean circulation model (OPA9) to represent the ocean biogeochemical processes (Aumont et al., 2015). PISCES model can be used for both regional and global simulations of lower trophic levels of the marine ecosystem and ocean carbon cycle (Bopp et al., 2005; Resplandy et al., 2012). The Earth System model of the Institute Pierre et Simon Laplace and Centre National de Recherche en Météorologie (IPSL-CNRM), which includes a full carbon cycle and uses PISCES to represent the ocean carbon cycle, contributed to CMIP5 (Séférian et al., 2013).

In this study, we present the performance of the ocean carbon cycle component in NUIST-CSM-2.0.1. In Section 2, we describe the NUIST-CSM-2.0.1 with a focus on the ocean carbon cycle component, as well as the setup of simulation experiments. We evaluate modeled biogeochemical fields against available observations in Section 3.1. In Section 3.2, we evaluate modeled oceanic uptake of anthropogenic CO_2 during the historical period against data-based estimates. In Section 3.3, we analyze modeled carbon-concentration sensitivity parameters and carbon-climate sensitivity parameters under different CO_2 concentration scenarios and compare our results with CMIP5 model results. Conclusions and discussions are presented in Section 4.

2 Method

2.1 Model

2.1.1 Framework of NUIST-CSM-2.0.1

Nanjing University of Information Science and Technology (NUIST) Climate System Model (NUIST-CSM) is a comprehensive Climate System Model that is designed to study interactions between different components of the climate system and its response to natural and anthropogenic forcing. NUIST-CSM-2.0.1 is developed based on the framework of NUIST-CSM v2.0 with active ocean biogeochemical cycle, while the physical components are the same as in NUIST-CSM v2.0. Compared with NUIST-CSM v1.0 (Cao et al., 2015), NUIST-CSM-2.0.1 includes more modifications and tuning in the dynamic component of the model to improve the simulated internal modes, such as El Niño–Southern Oscillation (ENSO), Madden–Julian oscillation (MJO), and monsoon (Li et al., 2017). The modifications are mainly related to the parameterizations of cloud microphysics, cumulus convection, Turbulent Kinetic Energy (TKE) schemes for the ocean and sea ice, freshwater/salt

fluxes, incorporation of the brine rejection in the ocean model, oceanic momentum viscosity, and sea ice albedos. We have modified the parameterization schemes and calibrated the parameters using constraints obtained from observation and physical understanding or empirical estimation. For example, the convective scheme was modified by introducing a boundary layer depth-dependent convective inhibition function, which significantly enhances the MJO eastward propagation and ENSO attributes.

Here we briefly introduce the main features of NUIST-CSM-2.0.1. NUIST-CSM-2.0.1 consists of three main component models, including *European Centre Hamburg Atmospheric Model* (ECHAM v5.3) (Roeckner et al., 2003), *Nucleus for European Modeling of the Ocean* version 3.4 (NEMO v3.4-revision 3814) (Madec and NEMO team, 2012) and *Los Alamos sea-ice model* version 4.1 (CICE v4.1) (Hunke and Lipsomb, 2010). The three component models are coupled by the Ocean-Atmosphere-Sea-Ice-Soil (OASIS v3.0) Model Coupling Toolkit (OASIS3-MCT) (Larson et al., 2005). The atmospheric resolution used in NUIST-CSM-2.0.1 is T42L31 which has a horizontal resolution of ~ 2.8° latitude by 2.8° longitude and 31 layers. The land surface is described by a simple surface scheme that is implicitly coupled with the atmosphere, in which surface fluxes and temperature are computed using an energy balance equation (Schulz et al., 2001). Surface albedo depends on the background state, including snow, forest, and canopy (Roesch et al., 2001). A simple mixed-layer lake scheme is also represented. Ocean component runs with the ORCA2 global ocean configuration, which is a type of tripole grid. It is based on a 2 degree Mercator mesh and has 31 layers with the thickness of ocean layer increasing from 10m in the upper ocean to 500m at 5000m depth. A local transformation is applied in the tropics to refine the resolution to up to 0.5 degree at the equator. In the ocean model, the incoming solar radiation is assumed to be able to penetrate to the upper ocean layers up to 391m, and bio-model penetration parameterization scheme is used to calculate the distribution of solar radiation. In that case, the penetration rate of solar radiation is dependent on modeled chlorophyll concentration in each ocean layer for the dynamic ocean circulation (Lengaigne et al., 2009). The sea-ice component includes four ice layers and one snow layer with a multi-layer thermodynamic scheme.

2.1.2 Ocean biogeochemical component

NUIST-CSM-2.0.1 employs the standard PISCES v2 to represent the ocean biogeochemical cycle in the atmosphere-ocean-sea-ice modeling system. The PISCES model is developed from a simple Nutrient-Phytoplankton-Zooplankton-Detritus (NPZD) model (Aumont et al., 2002). In the current version, there are 24 prognostic tracers in total, including dissolved inorganic and organic carbon, alkalinity, chlorophyll, and nutrients. We use the same biogeochemical parameter values as that used in Aumont et al. (2015). The only exception is the advection scheme for passive tracers. Here we use the Total Variance Dissipation (TVD) formulation instead of Monotone Upstream Scheme for Conservative Laws (MUSCL) formulation (Lévy et al., 2001a) to keep the advection scheme to be consistent with the one used in the physical ocean model.

Two different types of phytoplankton: nanophytoplankton and diatoms, and two size classes of zooplankton: mesozooplankton and microzooplankton, are presented in the model. The life cycle of phytoplankton is regulated by several processes, including growth, mortality, aggregation, remineralization, and grazing by zooplankton (Aumont et al., 2015). The growth rate of

phytoplankton is determined by temperature, photosynthetic active radiation, and availability of nutrients, including phosphate, nitrate, silicate, iron, and ammonium. The mortality rate of phytoplankton is set as a constant and is identical for nanophytoplankton and diatoms. The aggregations of nanophytoplankton only depend on the shear rate, which is set to 1 s^{-1} in the mixed layer and 0.01 below. The same is assumed for diatoms, while the aggregations of diatoms are further enhanced by the nutrients co-limitation. For all species, the phosphate, nitrate, and carbon are linked by a constant Redfield ratio. In NUIST-CSM-2.0.1, the Redfield ratio of C: N: P is set to be 122:16:1 (Takahashi et al., 1985) and the –O/C ratio is set to 1.34 (Kortzinger et al., 2001). In contrast, the Fe / C, Chlorophyll / C, and Silicon / C ratio are prognostically simulated by the model.

Since the Redfield ratio in the dissolved organic matter (DOM) are assumed to be constant, the DOM and dissolved organic carbon (DOC) is used indifferently. The remineralization of semi-labile DOC can occur in either oxic water or anoxic water that depend on the local oxygen concentration, and their degradation rates are specified and identical for oxic respiration and denitrification. Detritus is represented by different types, including particulate organism matter (POM), calcite, iron particles, and diatoms silicate. The sinking speed of detritus increases with depth. The POM is described by a simple two-compartment scheme, which uses two tracers corresponding to two size classes: a smaller class (POC: 1-100μm) and a larger class (GOC: 100-500μm). The sinking speed of GOC (50-200 m d^{-1}) is much faster than POC (3 m d^{-1}). Phytoplankton would be turned to the POM by the processes of mortality and aggregation. The fate of mortality and aggregation of nanophytoplankton depends on the proportion of the calcifying organisms. For nanophytoplankton, it is assumed that half of the calcifying organisms are associated with the shell. Because of the larger density of the calcite, 50% of the amount of the dying calcifiers is routed to the fast sinking particles. The same is assumed for the mortality of diatoms, and 50% of the dying diatoms is turned to the POM due to the larger density of biogenic silica. The degradation rate of the POM depends on the local temperature with a Q_{10} of about 1.9.

The geochemical boundary condition accounts for the external nutrient supply from five different sources, including atmospheric dust deposition of iron and silicon, river recharge of nutrients, dissolved carbon, and alkalinity, atmospheric deposition of nitrogen, and sediment mobilization of sedimentary iron. At the bottom of the ocean, different sediment parameterizations are applied to different tracers. The amount of permanently buried biogenic silica is assumed to balance the external source, the burial efficiency of POM is determined by the organic carbon sinking rate at the bottom follows the algorithm proposed by Dunne et al. (2007), and all the particulate iron would be buried into the sediment once they reach the ocean bottom. The amount of the unburied calcite and biogenic silica would dissolve back into the ocean water instantaneously. Carbonate chemistry including air-sea CO2 exchange is formulated based on the Ocean Carbon-Cycle Model Intercomparison Project (OCMIP-2) protocol (more information can be accessed at http://ocmip5.ipsl.jussieu.fr/OCMIP/). The quadratic wind-speed formulation proposed by Wanninkhof (1992) is used to compute the air-sea exchange of carbon and oxygen.

The NUIST-CSM-2.0.1 can be used to study interactions between climate change and marine biogeochemical with prescribed atmospheric CO_2 concentrations. However, in the current form, the model is not able to simulate fully coupled climate-carbon interactions with prescribed CO_2 emissions due to the lack of an interactive terrestrial carbon cycle component.

2.2 Simulations

First, NUIST-CSM-2.0.1 was spun up for 1500 years with all related parameters set to pre-industrial values including orbit parameters and greenhouse gas (GHGs) concentrations (280 ppm for CO_2, 720 ppb for CH_4, 270 ppb for N_2O, and 0 ppt for both CFC_{11} and CFC_{12}). The atmosphere and sea-ice components use current-day observations as initial conditions while the ocean component uses the end of a 600-year offline simulation as the initial state. Averaged over the last 100 years of the spin-up simulation, globally integrated sea-air CO_2 flux is -0.03 PgC yr^{-1}, and the linear drift is 0.0006 PgC yr^{-1} per year, indicating that a quasi-equilibrium state has been reached for the global ocean carbon cycle. Meanwhile, global mean SST averaged over the last 100 years of spin-up simulation is 13.1 Celsius (℃) with the linear drift of 0.001 ℃ per year, and ocean mean temperature 3.4 ℃ with the linear drift of 0.0004 ℃ per year, indicating that dynamic ocean component has also reached a quasi-equilibrium state.

Using the end of the 1500-year spin-up simulation as the initial state of the nominal pre-industrial year of 1800, the model is further integrated to year 2100 with prescribed time-series of atmospheric concentrations of GHGs, including CO_2, CH_4, N_2O, and CFCs and aerosols, and all other input forcings have remained at the pre-industrial level. From the year 1800 to 2008, we use the prescribed concentrations of GHGs a from observational records (http://www.mpimet.mpg.de/en/science/observations-data), and from the year 2009 to 2100, prescribed GHGs are taken from representative concentrations pathway RCP 8.5 (Moss et al., 2010) to represent a future world with intensive fossil fuel emissions. In addition, following the protocol of CMIP5 (Taylor et al., 2012), we performed an idealized 1%/yr CO_2 run (core 6.1 in CMIP5 experiment design), in which atmospheric CO_2 is increased at a rate of 1% per year starting from the end state of the pre-industrial control simulation with other GHGs concentration remaining at pre-industrial level. The simulation lasted for 140 years until atmospheric CO_2 concentration has quadrupled.

To separate the effect of atmospheric CO_2 and global warming on the ocean carbon cycle, we performed three types of experiments as summarized in Table 1 (biogeochemically coupled, radiatively coupled, and fully coupled). These types of simulations were also performed by previous studies that investigated the effect of CO_2 and CO_2-induced warming on the global carbon cycle (Friedlingstein et al., 2006; Arora et al., 2013; Schwinger et al., 2014).

1) Biogeochemically coupled (BC) simulations in which the code of the ocean carbon cycle sees changing atmospheric CO_2, but the code of atmospheric radiation sees the constant pre-industrial concentration of CO_2 and other GHGs as in the spin-up simulation. In this way, the ocean carbon cycle is only affected by changing atmospheric CO_2, but no direct effect of GHG-induced warming;

2) Radiatively coupled (RC) simulations in which the code of the ocean carbon cycle sees pre-industrial atmospheric CO_2, but the code of atmospheric radiation sees the changing concentrations of atmospheric CO_2 and other GHGs. In this way, the ocean carbon cycle is only affected by GHG-induced warming, but no direct effect of changing atmospheric CO_2.

3) Fully-coupled (FC) simulations in which both the codes of the ocean carbon cycle and atmospheric radiation see the changing concentrations of atmospheric CO_2 and other GHGs. In this way, the ocean carbon cycle is affected by changes in

both atmospheric CO_2 and GHG-induced warming.

In total, there are 7 different simulations in this study, including one fully coupled spin-up simulation for 1500 years, three historical+RCP8.5 runs (FC, BC, and RC) from 1800 to 2100, and three idealized 1%/yr CO2 runs (FC-1%, BC-1%, and RC-1%) for 140 years.

3 Results

Firstly, we make the comprehensive comparisons of 22 dynamic ocean fields covering the wind stress, heat flux, water flux, temperature, salinity, thermocline depth, mixed layer depth, and the Atlantic and global meridional overturning circulations. The results from the pre-industrial simulation (averaged over the last 100 years of the 1500 spin-up simulation) are compared with 18 top CMIP5 models, including BCC-CSM1-1, CCSM4, GFDL-ESM2M, HadGEM2-ES, IPSL-CM5A-LR, MPI-ESM-LR, NorESM1-M. The results from the FC simulation are compared with modern-era observations and reanalysis data. The figures are not shown but can be found in the supplementary material. The results show that NUIST-CSM-2.0.1 can reproduce reasonably realistic ocean circulations, climatology, and internal and coupled modes of variability. The assessment criteria are defined by the pattern correlation coefficient (PCC) and normalized root-mean-square error (NRMSE). The performances of more than half of the 22 fields simulated by NUIST-CSM-2.0.1 are ranked above average among the 18 CMIP5 models.

In particular, we compare the performance of NUIST-CSM-2.0.1 with IPSL-CM5A-LR, which also uses NEMO-PISCES system and ORCA2 configuration, but different atmospheric, land and sea-ice models and coupling strategy (Dufresne et al., 2013). In general, NUIST-CSM-2.0.1 and IPSL-CM5A-LR show similar skills in simulating dynamic ocean fields. NUIST-CSM-2.0.1 shows better skills in simulating the surface temperature, surface wind stress, meridional overturning circulation while IPSL-CM5A-LR shows better skills in simulating the mixed layer depth and salinity.

Besides, several biogeochemical fields are also compared between the NUIST-CSM-2.0.1 and IPSL-CM5A-LR from the pre-industrial simulations, including the geographic distribution averaged over the upper ocean (0-100m) and the zonally averaged latitude-depth distribution of macro-nutrients, alkalinity, and the DIC, as well as the geographic surface distribution of chlorophyll. The figures can be found in the supplementary material. The two models are shown to have similar skills in simulating the upper ocean biogeochemical climatology. The PCCs of the phosphate, nitrate, silicate, chlorophyll, and alkalinity fields are 0.93, 0.91, 0.83, 0.79, and 0.63, respectively. Compared with the IPSL-CM5A-LR, the NUIST-CSM-2.0.1 shows fewer skills in simulating chlorophyll concentration in the Arctic Ocean and the maximum zone of the macro-nutrients and DIC in the deep Pacific Ocean. However, the IPSL-CM5A-LR shows a wrong pattern of the latitude-depth distribution of alkalinity in the deep ocean, which is simulated better in the NUIST-CSM-2.0.1.

3.1 Evaluation of NUIST-CSM-2.0.1 simulated present-day ocean biogeochemistry

In this section, we compare model-simulated ocean biogeochemical fields that are directly related to the ocean ecosystem and carbon cycle, including nutrients, chlorophyll, and net primary production (NPP), against available data-based estimates. A

brief description of the observational data and data-based estimates used is given in Appendix A. To allow a direct comparison between NUIST-CSM-2.0.1 results and observations, we interpolate NUIST-CSM-2.0.1 results onto the corresponding grids of observational data using the distance-weighted averaged remapping method.

Nutrients play vital roles in the ocean biogeochemical cycles. A lack of nutrients would limit the growth of phytoplankton. Figure 1 compares model-simulated annual mean spatial distributions of macro-nutrients, including nitrate (NO_3^-), phosphate (PO_4^{3-}), and silicate (SiO_4^{2-}) averaged above the top 100m depth during the 1990s against WOA09 observations during the same period (Garcia, et al., 2010). The model reproduces reasonably well the large-scale pattern of upper ocean macro-nutrient distributions (Fig. 1). Relatively high nutrient concentrations are found in the Southern Ocean, subarctic Pacific Ocean, and the mid-east Pacific Ocean where strong vertical mixing and upwelling bring nutrient-rich deep water to the surface (Whitney, 2011). Relatively low concentrations of nutrients are found in subtropical regions where the vertical mixing between surface and the deep ocean is relatively weak. Some noticeable discrepancies between model results and observations are noticed. The macro-nutrients concentrations are overestimated near 45°S but underestimated along Antarctica, which may be associated with the upwelling bias in these regions. Besides, an overestimate of silicate concentration is found in the whole mid-low latitude Pacific Ocean. Since phosphate and nitrate concentrations are simulated well in this region, the discrepancy of surface silicate concentration is probably associated with an underestimate of diatoms uptake or a too strong dissolution rate of biogenic silica.

Figure 2 shows the zonal mean latitude-depth distribution of macro-nutrients during the 1990s and WOA09 observations in the Pacific Ocean, Atlantic Ocean, and the global ocean. In general, the pattern of silicate is simulated well in the whole ocean, but some discrepancies are found in the high latitude regions, such as the underestimated maximum zone of silicate in the northern Pacific Ocean at about 2000m depth and underestimation in the bottom of the Southern Ocean. However, compared to observations, phosphate and nitrate are overestimated in the deep Pacific Ocean, which is probably a result of too deep remineralization of organic matters in the ocean interior. Also, a too sluggish deep ocean circulation may partly account for the overestimated macro-nutrients concentrations in the deep Pacific Ocean. The inclusion of natural radiocarbon (^{14}C) in the model, which is not implemented yet, would be useful in separating the effect of modeled ocean dynamics and biology (Stocker and Wright, 1996). We will further discuss this issue in Section 4.

Figure 3 shows the modeled spatial distribution of annual mean surface chlorophyll concentration during the 1990s compared with SeaWiFS observational data (Behrenfeld and Falkowski, 1997a, 1997b.). The model simulates reasonably well the large-scale pattern of ocean surface chlorophyll concentration with high levels of chlorophyll in the subarctic Pacific Ocean, North Atlantic Ocean, equatorial Pacific, and low levels of chlorophyll in subtropical ocean. NUIST-CSM-2.0.1 simulates relatively high chlorophyll concentrations along the extratropical (except the Arctic Ocean) coastal regions, but compared to observations, the model generally underestimates chlorophyll concentration in the tropical coastal regions, especially in the tropical Indian Ocean and the Atlantic Ocean. This underestimation is probably associated with the deficiencies in modeled coastal dynamics, which is usually not represented well by the relatively coarse resolution global ocean models (Aumont et al., 2015). It is reported that the observed chlorophyll distribution is better reproduced when PISCES is coupled to a higher resolution ocean

circulation model (Lee et al., 2000; Hood et al., 2003; Kone et al., 2009). In the Southern Ocean where the seawater is typically characterized by high nutrients and low chlorophyll (Lin et al., 2016), the model overestimates chlorophyll concentration when compared with satellite-derived observations. Previous studies pointed out that chlorophyll concentrations derived from reflectance by standard algorithms tend to be underestimated by a factor of about 2 to 2.5, especially in intermediate concentration regions such as the Southern Ocean (Garcia et al., 2005; Kahru and Mitchell, 2010). Therefore, the overestimation of chlorophyll concentration by NUIST-CSM-2.0.1 in the Southern Ocean may partly be explained by the underestimation of satellite-derived chlorophyll.

We next present model-simulated pattern of nutrient limitation. In the model, the nutrients limitation coefficient (0~1) is computed from the Michaelis-Menten equation. We first calculate the annual mean nutrient limitation coefficient for each type of nutrients (phosphate, nitrate, silicate, and iron), and the nutrient with the lowest limitation coefficient is regarded as the factor that most limits phytoplankton growth. Temperature and light are assumed to be the most limiting factor when all nutrients are sufficient for phytoplankton growth and all nutrient limitation coefficients are larger than 0.9. As shown in Fig. 4, the limitation pattern of the nanophytoplankton and diatoms are similar in the middle to low latitude oceans. In the equatorial Pacific Ocean and the Southern Ocean that is usually regarded as high nutrient and low chlorophyll regions, iron is the most limiting nutrient for both nanophytoplankton and diatoms. Nitrate is the most limiting factor in the subtropical Pacific Ocean, while the phosphate is the most limiting factor in the Indian Ocean and in the middle to low latitude in the Atlantic Ocean. In the high latitude ocean, nanophytoplankton is mostly limited by the available light and temperature, while diatoms are mostly limited by the silicate. The model-simulated limitation pattern is generally consistent with the results diagnosed from IPSL-CM5A-LR, except that the most limiting factor in the Indian Ocean and the Atlantic Ocean is phosphate in this study while it is nitrate in IPSL-CM5A-LR (Schneider et al., 2008).

The net primary production (NPP) of phytoplankton in NUIST-CSM-2.0.1 is calculated as a function of the chlorophyll concentration, nutrient availability, ocean temperature, and the photosynthetically active radiation (PAR). Here we compare modeled NPP with a data-based estimate (http://www.science.oregonstate.edu/ocean.productivity/index.php) that is calculated as a function of the sea surface temperature, PAR, and the SeaWiFS chlorophyll concentrations based on the Vertically Generalized Production Model (VGPM) which was first proposed by Behrenfeld and Falkowski (1997a, 1997b) (Fig. 5). NUIST-CSM-2.0.1 well reproduces the relatively high NPP in the eastern tropical Pacific, subarctic Pacific, and the North Atlantic. Major discrepancies are seen in the central tropical Pacific, North Atlantic, and the Arctic regions. The overestimation of the NPP in the central tropical Pacific is probably related to the model's bias in the simulation of the Pacific cold tongue, which is also shifted westward with overestimated intensity (Cao et al., 2015). NPP is underestimated in the North Atlantic, Arabian Sea, subarctic North Pacific and Arctic coastal regions, which is likely related to the model's underestimation of coastal upwelling in these regions. Averaged over the 1990s, globally integrated ocean NPP from the NUIST-CSM-2.0.1 simulation is 41.5 PgC yr^{-1}, compared with the data-based estimates of 37 to 67 PgC yr^{-1}. The large range of data-based estimates of global NPP is a result of different satellite observations and different algorithms for the NPP estimation (Longhurst et al., 1995; Antoine et al., 1996; Behrenfeld and Falkowski, 1997b; Behrenfeld et al., 2005). Global NPP simulated by CMIP5

models also shows a wide range of values from 30.9 to 78.7 PgC yr^{-1} (Bopp et al., 2013). NUIST-CSM-2.0.1 simulated value of global NPP is within the range of data-based estimates and current model simulations. Of the NUIST-CSM-2.0.1 simulated global ocean NPP, 19% is contributed by diatoms, and 81% is contributed by nanophytoplankton. For comparison, from the data-based estimate, 7%% to 32% of the total NPP is associated with diatoms (Uitz et al.,2010; Hirata et al., 2011), and ocean biogeochemical models estimate that 15% to 30% global NPP is from diatoms (Aumont et al., 2003; Dutkiewicz et al., 2005; Yool and Popova, 2011).

The spatial resolution of the oceanic component of NUIST-CSM-2.0.1 is relatively coarse, especially in high latitudes. It is reported that an ocean model with higher spatial resolution would produce a larger NPP as mesoscale and submesoscale processes would significantly enhance ocean biological productivity (McGillicuddy et al., 1998; Oschlies and Garçon, 1998; Lévy et al., 2001b). Also, coastal regions would be better presented in a higher resolution model.

Figures 6 and 7 display the modeled and observed alkalinity and DIC averaged over the upper ocean (0-100m) and along zonally averaged section in the Pacific Ocean, the Atlantic Ocean, and the global ocean. The observed large-scale pattern of the DIC is simulated well (pattern correlation coefficient PCC=0.91), while the model has a moderate skill in simulating the geographic distribution of the upper ocean alkalinity (PCC=0.68). The large-scale pattern of the zonal averaged latitude-depth distribution of both DIC and alkalinity is reasonable in the Atlantic Ocean and global ocean. However, the model-simulated DIC and alkalinity distribution in the Pacific Ocean is relatively poor. One salient pattern of observed DIC and alkalinity distribution is that their maximum concentrations are around 2000-3000m of the North Pacific Ocean, which the model fails to simulate well. The model also overestimates DIC storage in the deep Pacific Ocean. The mismatch between model-simulated and observed DIC and alkalinity concentrations (underestimation of DIC and alkalinity concentrations in the upper ocean (above ~ 1000 m) and overestimation of their concentrations in the deep ocean) resemble those of the nitrate and phosphate.

3.2 Evaluation of NUIST-CSM-2.0.1 simulated ocean carbon cycle with observations

Here we compare NUIST-CSM-2.0.1 simulated sea-air CO_2 flux and oceanic uptake of atmospheric CO_2 during the historical period (FC) against available observations.

We compare model-simulated sea-air CO_2 flux against the observation-based estimate for the reference year 2000 (Takahashi et al., 2009). Sea-air CO_2 flux in NUIST-CSM-2.0.1 is calculated following the OCMIP-2 protocol and is defined as:

$$\mathrm{F} = K_w \times S_A \times (P_{\mathrm{W}} - P_{\mathrm{a}}) \quad (1)$$

Where K_w is the CO_2 gas transfer coefficient calculated as a function of wind speed, S_A is the solubility of CO_2 at the sea surface, and P_a and P_w are CO_2 partial pressure in the overlying atmosphere and sea surface, respectively. Defined in this way, a positive value of F represents CO_2 flux from ocean to the atmosphere.

As shown in Fig. 8, NUIST-CSM-2.0.1 realistically reproduces the large-scale pattern of observed sea-air CO_2 flux with CO_2 outgassing in the equatorial oceans and uptake in the mid-to-high latitude oceans. For both the observation and model simulations, strong CO2 uptake is inspected in the North Atlantic Ocean where sea surface temperature is low and formation

of deep water is active. It appears that the model overestimates both the amount and the westward extension of CO_2 outgassing in the equatorial Pacific Ocean. Based on Eq. (1), sea-air CO_2 flux is related to three factors: surface wind speed, CO_2 solubility, and the partial pressure difference between ocean and atmosphere ($dpCO_2$). As expected, the global pattern of sea-air CO_2 flux is mainly determined by the simulated difference in CO_2 pressure ($dpCO_2$). The model simulates an excessive upwelling in the mid-western equatorial Pacific Ocean. The overestimated transport of DIC-enriched deep water to the surface increases the dpCO2 and then leads to the overestimated sea-air CO2 flux in this region. Meanwhile, wind speed in the equatorial Pacific Ocean is overestimated relative to observations (Cao et al., 2015), which also contributes to the overestimated sea-air CO_2 flux in this region. Integrated over the global ocean, NUIST-CSM-2.0.1 simulated oceanic CO_2 uptake for the year 2000 is 1.7 PgC, comparing well with the data-based estimate of 1.6 ± 0.9 PgC (Takahashi et al., 2009).

Now we compare model-simulated ocean storage of anthropogenic CO_2 during the 1990s (i.e. the excess DIC relative the pre-industrial value) with data-based estimates from GLODAP (Key et al., 2004) in terms of both latitude-depth distribution (Fig. 9a, c) and vertically integrated column inventory (Fig. 9b, d). NUIST-CSM-2.0.1 reasonably captures the data-based large-scale distribution of anthropogenic CO_2. As pointed out by Sabine et al., (2004), deep penetration of anthropogenic CO_2 is typically associated with convergence zones at temperate latitudes and high latitude oceans where vertical mixing is strong. For both data-based estimates and model simulations, a substantial amount of anthropogenic CO_2 has penetrated down to the ocean interior as deep as 1000 m with two penetration tongues near 30°N and 40°S. NUIST-CSM-2.0.1 also reasonably reproduces the realistic large-scale pattern of the vertically integrated column inventory of anthropogenic CO_2 with the largest storage in the North Atlantic Ocean. However, the model appears to overestimate the carbon storage in the Northern Pacific Ocean.

We also calculated the present-day anthropogenic CO_2 budget over different periods (the 1980s, 1990s, 2000s, 2002-2011, and from pre-industrial to 2011) and compared NUIST-CSM-2.0.1 simulated results against the data-based estimate provided by Intergovernmental Panel on Climate Change Fifth Assessment Report (IPCC AR5) (Table 2). The model-simulated ocean uptake of anthropogenic CO_2 is slightly lower than that from IPCC AR5 but within the estimated uncertainty range. For example, from the pre-industrial time to the year 2011, NUIST-CSM-2.0.1 simulated cumulative oceanic CO_2 uptake is 144 PgC, compared with data-based estimates of 155 ± 30 PgC.

Figure 10 compares the spatial pattern of NUIST-CSM-2.0.1 simulated carbon-related fields with corresponding observations using Taylor diagrams (Taylor, 2001). Model-simulated statistical patterns of surface nitrate and phosphate compares well with observations with correlation coefficients r>0.9 and normalized standard deviation (SD) close to 1.0. However, the simulated spatial pattern of surface silicate shows larger deviations from the observations. The simulated spatial pattern of chlorophyll and NPP compare poorly with observations with a correlation of 0.45 and 0.40, respectively. The simulated spatial pattern of sea-air CO2 flux compares reasonably well with observations with a correlation coefficient of 0.75 and a normalized SD close to 1. It is noted that chlorophyll, NPP, and sea-air CO2 flux are not directly observed but diagnosed from observation-based data, and thus their estimations are subject to considerable uncertainties.

3.3 Response of the oceanic CO2 uptake to atmospheric CO2 and global warming

Increasing atmospheric CO_2 affects sea-air CO_2 flux directly and thus oceanic CO_2 uptake. Meanwhile, CO_2-induced warming also affects the ocean carbon cycle via changes in climatic fields such as temperature and ocean circulation. In this section, we first present NUIST-CSM-2.0.1 simulated physical climate change and oceanic CO_2 uptake under the prescribed atmospheric CO_2 concentration pathway of the RCP 8.5 scenario. We then present NUIST-CSM-2.0.1 simulated oceanic CO_2 uptake in the idealized simulations with a 1% per year increase in atmospheric CO_2.

3.3.1 NUIST-CSM-2.0.1 simulated physical climate change under RCP 8.5

Figure 11 shows NUIST-CSM-2.0.1 simulated changes (relative to pre-industrial level) in global annual mean surface air temperature (SAT), mixed layer depth (MLD), and the intensity of Atlantic meridional overturning circulation (AMOC) at 30°N from 1900 to 2100 under the historical and RCP8.5 scenario. In the simulation of FC, NUIST-CSM-2.0.1 simulated annual mean of the global mean SAT anomaly over the period of 2080 to 2100 (relative to the period of 1986-2005) is 4.0K, which is within the range of CMIP5 model results of 3.7±0.7K under the RCP 8.5 scenario (Collins and Knutti, 2013; Knutti and Sedláček, 2013). With increasing atmospheric temperature, the global ocean also becomes warmer in FC and RC simulations, reducing CO_2 solubility and acting to mitigate oceanic CO_2 uptake.

MLD and AMOC show much stronger interannual fluctuations than SAT while both of them show a long-term trend of decrease. The reduction of mixed layer depth, which is associated with a relatively faster warming of the surface ocean and a slower response of the deep ocean, indicates a more stratified upper ocean with global warming (Held et al., 2010). At the pre-industrial time, model-simulated AMOC index at 30°N is 24 Sv ($1Sv = 10^6\ m^3\ s^{-1}$), compared with the value of 14 to 31 Sv from CMIP5 models (Weaver et al., 2012). The modeled annual mean of AMOC transport at 30°N averaged from 2004 to 2011 is 20.7 Sv while the observation record during the same period from RAPID/MOCHA (Rapid Climate Change programme / Meridional Ocean Circulation and Heatflux Array) is 17.5 ± 3.8 Sv (Rhein et al., 2013). A substantial weakening of AMOC intensity in the RC and FC simulations is seen in the 21st century under the RCP8.5 scenario, which is associated with ocean surface warming and increased freshwater input into the North Atlantic (Gregory et al., 2005). By 2100, the simulated intensity of AMOC declines to about half its pre-industrial value. The simulated 54% weakening of AMOC by the end of this century is at the higher end of what is simulated by CMIP5 models that range from 15% to 60% under the RCP 8.5 scenario (Cheng et al., 2013).

3.3.2 NUIST-CSM-2.0.1 simulated oceanic CO_2 uptake under RCP 8.5

The ocean carbon cycle is regulated by changes in atmospheric CO2 and physical climate (Doney et al., 2004). In the FC simulation, weakening of vertical ocean mixing, as indicated by the reduced mixed layer depth and weakening of AMOC, will reduce the vertical transport of CO_2 from the upper ocean to ocean interior, and thus reduce oceanic CO_2 uptake. A warmer surface ocean would reduce CO_2 solubility, also reducing oceanic CO_2 uptake.

Figure 12 shows the time evolution of model-simulated oceanic CO_2 uptake for the simulations BC, RC, FC, and the linear sum of BC and RC. In the BC simulation, only increasing atmospheric CO_2 affects the ocean carbon cycle. By the year 2100, the global ocean has absorbed a total of 604 PgC of anthropogenic CO_2 from the atmosphere. In the RC simulation, constant atmospheric CO_2 is seen by the ocean carbon cycle, and the atmospheric radiation code sees increasing atmospheric CO_2 concentration. As discussed above, increasing sea surface temperature, enhancing ocean stratification, and reduced AMOC all act to decrease CO_2 uptake. As a result, CO_2-induced warming alone causes the ocean to release CO_2 into the atmosphere. By the year 2100, the modeled cumulative CO_2 uptake is -37.6 PgC. In the FC simulation, oceanic CO_2 uptake is affected by both the increase in atmospheric CO_2 and CO_2-induced global warming. By the end of the 21st century, simulated cumulative oceanic CO_2 uptake since pre-industrial era is 516 PgC, which is close to the median of ~500 PgC from CMIP5 models under the same RCP 8.5 scenario (Jones et al., 2013).

As seen from Figure 12, the sum of the simulated oceanic CO_2 uptake from the BC and RC simulations (566 PgC) is larger than that from the FC run (516 PgC), indicating that the effect of increasing atmospheric CO_2 (carbon-concentration sensitivity) and the effect of global warming (carbon-climate sensitivity) on the oceanic CO_2 uptake is not exactly additive. This nonlinearity was also found in previous studies (Boer and Arora, 2009; Gregory et al., 2009; Schwinger et al., 2014). The NUIST-CSM-2.0.1 simulated nonlinearity (discrepancy between the sum of the carbon-concentration sensitivity and the carbon-climate sensitivity and the total carbon uptake in the fully-coupled run, i.e., BC+RC-FC) is 50.4 PgC by the end of the 21st century. This nonlinearity is about 9.8% of the total ocean uptake, and it is larger than the magnitude of the radiative effect on ocean carbon uptake (-37.6 PgC).

To better understand oceanic CO_2 uptake in response to changing atmospheric CO_2 and CO_2-induced warming, Figure 13 shows the spatial distribution of anthropogenic sea-air CO_2 flux at the end of the 21st century (averaged over the year 2091 to 2100) under the RCP8.5 scenario for FC, RC, and BC simulations, and the difference between the FC simulation and the sum of the RC and BC simulations.

In the BC simulation, the ocean absorbs atmospheric CO_2 in most regions except for a few scattered grid points of the Pacific Ocean at the mid-latitudes with slight CO_2 outgassing. The strongest CO_2 uptake is seen in the North Atlantic and the Southern Ocean. Results from the RC simulation show CO_2 outgassing in large parts of the global ocean as a result of CO_2-induced warming that reduces the CO_2 solubility and increases the oceanic pCO_2. In the Arctic Ocean, warming induces a net uptake of CO_2 as a result of reduced sea-ice extent under global warming, which allows more open seawater to absorb atmospheric CO_2. The FC simulation shows the combined effect of increasing atmospheric CO_2 and CO_2-induced warming on the oceanic CO_2 uptake (Fig 13c). Positive oceanic CO_2 uptake is simulated in most regions, indicating the dominant role of the increasing atmospheric CO_2 on the oceanic carbon uptake. Similar to the BC simulation, the strongest CO_2 uptake is simulated in the North Atlantic and the Southern Ocean. CO_2 outgassing is seen in the subtropical Pacific Ocean, indicating that the radiative effect dominates biogeochemical effect in this region.

Figure 13d shows the spatial distribution of the difference in sea-air CO_2 flux between the FC simulation and the sum of the BC and RC simulations during the 2090s. The difference represents the nonlinearity between carbon-climate sensitivity and

carbon-concentration sensitivity. In NUIST-CSM, relatively large nonlinearity is seen in the northern North Atlantic Ocean and Southern Ocean (especially the southern South Atlantic), which is consistent with the findings of previous studies (Zickfeld et al., 2011; Schwinger et al., 2014). The effect of the background simulation can partly explain the nonlinearity. Compared with the radiatively coupled simulation, more carbon is subject to the effect of climate change in fully coupled simulations. As a consequence, in fully coupled simulations, the increased temperature would have a larger effect on CO_2 solubility and buffer factor. Also, reduced ocean circulation and increased ocean stratification would slow down the transport of anthropogenic CO2 from the surface to the deep ocean. Thus, compared to the RC simulation, slowing ocean ventilation would cause a larger reduction in oceanic CO_2 uptake in the FC simulation. The oceanic carbon uptake in the fully-coupled simulations is lower than the sum of the BC and RC simulations, which is consistent with other CMIP5 models (Schwinger et al., 2014).

3.3.3 carbon-concentration and carbon-climate sensitivity parameters diagnosed from NUIST-CSM-2.0.1

We further investigate mode-simulated oceanic CO2 uptake under the framework of the carbon-concentration and carbon-climate sensitivity parameters. Friedlingstein et al. (2006) proposed that cumulative oceanic CO_2 uptake can be decomposed approximately using the linear sum of carbon-concentration sensitivity and carbon-climate sensitivity:

$$\int_0^t F'\,dt \approx \gamma \Delta T + \beta \Delta C_A \quad (2)$$

Where F' is the oceanic carbon uptake and $\int_0^t F'\,dt$ represent the cumulated ocean carbon uptake. ΔT is the change in global mean surface air temperature. γ and β represent the sensitivity of ocean carbon storage to CO_2-induced warming and atmospheric CO2 concentration, respectively.

Based on Eq., (2), Arora et al., (2013) diagnosed these two parameters from two types of experiments performed by a subset of CMIP5 models, i.e. biogeochemically-coupled simulations and radiatively-coupled simulations.

In the biogeochemically-coupled simulations where the ocean carbon uptake is only affected by changing atmospheric CO_2, Eq. (2) can be simplified as:

$$\int_0^t F'\,dt \approx \beta \Delta C_A \quad (3)$$

Where F' represent oceanic carbon uptake change in the biogeochemically coupled simulation. In the radiatively-coupled simulations where the ocean carbon uptake is only affected by CO_2-induced warming. Eq. (2) can be simplified as:

$$\int_0^t F'\,dt \approx \gamma \Delta T \quad (4)$$

Where F' represent oceanic carbon uptake change in the radiatively coupled simulation.

In this study, we estimate the sensitivity parameters of carbon-concentration and carbon-climate sensitivities following Arora et al., (2013) using equations (3) and (4). Figure 14 shows the change in ocean carbon storage against the change in the atmospheric CO_2 concentration (Fig. 14a) and the global annual mean surface temperature (Fig. 14b), respectively. The derived evolution of carbon-concentration sensitivity parameter β as a function of atmospheric CO_2 concentration and carbon-climate sensitivity parameter γ as a function of the change in temperature is shown in Fig. 14c and 14d, respectively. As shown in Fig. 14a, in the BC and RC simulations modeled ocean storage of anthropogenic CO_2 scales roughly linearly

with atmospheric CO_2 and changes in global mean surface temperature. Increasing atmospheric CO_2 alone increases oceanic CO_2 uptake whereas increasing temperature alone decreases CO_2 uptake. Therefore, the carbon-climate parameter γ is negative while the carbon-concentration parameter β is positive (Fig. 14). From 1950 to 2100, the magnitude of carbon-climate parameter increases with time, indicating that with enhanced warming, each degree of surface temperature increase would induce more CO_2 outgassing from the ocean (Fig 14d). Carbon-concentration parameter initially increases with atmospheric CO_2, and then slightly decreases (Fig. 14c). The decreasing trend of β is consistent with the slowdown of the increasing trend of oceanic CO_2 uptake at the end of the 21st century as a result of decreased oceanic buffer ability due to the increasing DIC concentration. Similar trends of carbon-climate and carbon-concentration sensitivity parameters are found in the previous studies (Arora et al., 2013). The increased sensitivity of CO_2 outgassing to increasing temperature and the decreased sensitivity of CO_2 uptake to increasing atmospheric CO_2 indicate that ocean's ability to absorb atmospheric CO2 would be weakened with increasing atmospheric CO2 and global warming.

3.3.4 Carbon-concentration and carbon-climate sensitivity parameters from 1% per year CO_2 simulations

Arora et al., (2013) analyzed carbon-concentration and carbon-climate sensitivity parameters from CMIP5 models using the benchmark simulations in which atmospheric CO_2 is assumed to increase at a rate of 1% per year for 140 years to reach 4× CO_2. To have a direct comparison with CMIP5 results, we performed another set of simulations under the same CO_2 concentration pathway.

Figure 15 shows the time evolution of model-simulated oceanic CO_2 uptake for the simulations of BC, RC, FC, and the linear sum of BC and RC in 1% per year CO_2 increase experiments. To some extent, Figure 15 shows the similar time evolution of model-simulated oceanic CO_2 uptake under the RCP 8.5 scenario as shown in Figure 12. It is reported that the nonlinearity between carbon-climate and carbon-concentration sensitivities accounts for 3.6% -10.6% of the total ocean carbon uptake for CMIP5 models in 1% per year CO_2 increase experiments (Schwinger et al., 2014). For comparison, at the end of the 1% per year CO_2 increase simulations, nonlinearity diagnosed from NUIST-CSM-2.0.1 is 9.6% (57 PgC) of the total oceanic CO_2 uptake, which is at the higher end of the nonlinearity magnitude estimated by CMIP5 models.

We compare NUIST-CSM-2.0.1 simulated carbon-concentration and carbon-climate parameters with those of CMIP5 results in Fig. 16. At the end of 1% increasing CO_2 simulation, the diagnosed value of β from CMIP5 models ranges from 0.69 to 0.91 PgC/ppm with a multi-model mean value of 0.80 PgC/ppm. For comparison, the carbon-concentration sensitivity parameter diagnosed from NUIST-CSM-2.0.1 simulations with a 1% per year increase in atmospheric CO_2 is 0.81 PgC/ppm at the end of the simulation. Compared to the carbon-concentration sensitivity parameter, the model-simulated carbon-climate sensitivity parameter has a much larger range among CMIP5 models, with values ranging from -2.4 to -12.1 PgC/K at the end of the simulations. The larger spread of the carbon-climate sensitivity parameter is associated with the spread of the model-simulated climate change and the dependency of carbon cycle processes on climate change. The mean value of the carbon-climate sensitivity parameter from CMIP5 models is -7.8 PgC/K. For comparison, at the end of the simulation, the NUIST-CSM-2.0.1 simulated value of carbon-climate parameter γ with the scenario of 1% per year increase in atmospheric CO_2 is -7.1 PgC/K.

These results indicate that NUIST-CSM-2.0.1 simulated response of oceanic CO_2 uptake to atmospheric CO_2 and CO_2-induced warming is in general agreement with ensemble means of the CMIP5 models.

4 Discussion and conclusion

In this study, we evaluated the performance of the NUIST Climate System Model (NUIST-CSM-2.0.1) in simulating the present-day ocean carbon cycle. We also investigated the model-simulated oceanic CO_2 uptake in response to the individual and combined effect of increasing atmospheric CO_2 and CO2-induced global warming.

The model simulates reasonably well the large-scale patterns of upper ocean nutrient concentrations including nitrate, phosphate, and silicate. The model also reasonably reproduces observed large-scale distribution of chlorophyll, alkalinity, DIC, and ocean net primary production (NPP). The integrated global ocean NPP simulated by NUIST-CSM-2.0.1 is 42 PgC yr^{-1}, compared with observation-based estimates that range from 37 to 67 PgC yr^{-1} and CMIP5 model simulated results that range from 31 to 79 PgC yr^{-1}. The NUIST-CSM-2.0.1 simulated cumulative anthropogenic CO_2 uptake from the pre-industrial time to the year 2011 is 144 PgC, comparing well with data-based estimates of 155 ± 30 PgC during the same period (Ciais et al., 2013).

As proposed by Friedlingstein et al. (2006), the response of oceanic CO_2 uptake can be decomposed by the sum of two components, the response to increasing atmospheric CO_2 alone (carbon-concentration sensitivity parameter) and the response to CO_2-induced warming alone (carbon-climate sensitivity parameter). In the simulation where atmospheric CO_2 increases by 1% per year, by year 140, the NUIST-CSM-2.0.1 simulated carbon-concentration sensitivity parameter is 0.8 PgC/ppm, and carbon-climate sensitivity parameter is -7.1 PgC/K, indicating that increasing atmospheric CO_2 alone increases oceanic CO_2 uptake while global warming alone decreases oceanic CO_2 uptake. These estimated sensitivity parameters are in broad agreement with those estimated by CMIP5 models that yield carbon-concentration sensitivity parameters ranging from 0.7 to 0.9 PgC/ppm and carbon-climate sensitivity parameters ranging from -2.4 to -12.1 PgC/K.

Our simulations show that the sum of oceanic CO_2 uptake in response to changes in atmospheric CO_2 alone and CO_2-induced warming alone is somewhat larger than the oceanic CO_2 uptake in response to the combined effect of the two. The difference between the total oceanic CO_2 uptake and the linear sum of carbon-concentration sensitivity and carbon-climate sensitivity indicates the nonlinear sensitivity. In the NUIST-CSM-2.0.1 simulation with 1% per year increase in atmospheric CO_2, by year 140, the nonlinearity is 9.6% of the total oceanic CO_2 uptake. For comparison, nonlinearity from CMIP5 models accounts for 3.6% to 10.6% of the total oceanic CO_2 uptake.

While the results presented here show some success of the NUIST-CSM-2.0.1 model in the simulation of the ocean biogeochemistry and CO_2 uptake, we note a number of deficiencies in the modeled ocean carbon cycle. Both the simulated NPP and sea-air CO_2 flux have large biases in the equatorial Pacific (Fig. 5 and 8), which are likely associated with the model's bias in simulated SST and upwelling. The simulated Pacific cold tongue is shifted westward compared with observations (Cao et al., 2015), implying that the upwelling also shifts westward (Jin 1996; Li and Xie 2014). Besides, other noticeable

mismatches are seen between observations and model simulations, including overestimation of nitrate, phosphate, DIC, and alkalinity in the deep Pacific Ocean, underestimation of chlorophyll concentration along the tropical coastal regions, and.underestimation of NPP in high latitude regions.

In the future, NUIST-CSM, together with its ocean carbon cycle component, will be further improved. To better evaluate the NUIST-CSM simulated ocean dynamics and the ocean carbon cycle, the simulation of natural and bomb ^{14}C will be implemented since their distribution in the ocean is a good indicator of the strength of ocean mixing and deep ocean circulation (Levin and Vago, 2000; Matsumoto 2007; Skinner et al., 2017). Also, the model appears to underestimate the concentration of chlorophyll and NPP in the tropical coastal regions as a result of a relatively low model resolution, which cannot capture well coastal processes. The development of a higher-resolution (~10km) NUIST-CSM is planned, which could better capture the mesoscale processes and coastal dynamics (Griffies et al., 2015). Furthermore, in the latest version of NUIST-CSM, we upgrade the atmospheric and land surface model components to include a terrestrial carbon cycle (Cao et al., 2018). The new NUIST-CSM model with both land and ocean carbon cycle included can be used to investigate interactive feedbacks between climate change and the global carbon cycle.

Code and data availability.

The source code of NUIST-CSM-2.0.1, together with all input data are saved in one compressed file, which can be downloaded from https://doi.org/10.5281/zenodo.1184747 after registration. Also, a user guide describing the installation instructions, driver scripts, and software dependencies can be found in the repository at the same link. The simulation results illustrated in this study can be made available upon request to the authors.

Author contributions. Yifei Dai and Long Cao performed the simulations, analyzed the experiments, and made the figures. The NUIST ESM team led by Bin Wang provided the code of NUIST-CSM-2.0.1 used in this study and Bin Wang provided helpful discussions. Yifei Dai, Long Cao, and Bin Wang all contributed to the writing of the manuscript.

Acknowledgement. Long Cao is supported by the National Natural Science Foundation of China (41675063; 41422503). Bin Wang acknowledges the support by the Nanjing University of Information Science and Technology through funding the joint China-US Atmosphere-Ocean Research Center at the University of Hawaii. Yifei Dai acknowledges the support by the China Scholarship Council by providing a scholarship under the State Scholarship Fund. This is the ESMC publication number XXX and IPRC publication number YYYY.

Reference

Antoine, D., André, J.M. and Morel, A.: Oceanic primary production: 2. Estimation at global scale from satellite (Coastal Zone Color Scanner) chlorophyll. Global Biogeochemical Cycles, 10(1), 57-69, 1996.

Arora, V.K., Boer, G.J., Friedlingstein, P., Eby, M., Jones, C.D., Christian, J.R., Bonan, G., Bopp, L., Brovkin, V., Cadule, P.

and Hajima, T.: Carbon–concentration and carbon–climate feedbacks in CMIP5 Earth system models. Journal of Climate, 26(15), 5289-5314, 2013.

Aumont, O., Belviso, S. and Monfray, P.: Dimethylsulfoniopropionate (DMSP) and dimethylsulfide (DMS) sea surface distributions simulated from a global three‐dimensional ocean carbon cycle model. Journal of Geophysical Research: Oceans, 107(C4), 2002.

Aumont, O., Maier-Reimer, E., Blain, S. and Monfray, P.: An ecosystem model of the global ocean including Fe, Si, P colimitations. Global Biogeochemical Cycles, 17(2), 1060, 2003.

Aumont, O., Éthé, C., Tagliabue, A., Bopp, L. and Gehlen, M.: PISCES-v2: an ocean biogeochemical model for carbon and ecosystem studies. Geoscientific Model Development, 8(8), 2465-2513, 2015.

Ballantyne, A.P., Alden, C.B., Miller, J.B., Tans, P.P. and White, J.W.C.: Increase in observed net carbon dioxide uptake by land and oceans during the past 50 years. Nature, 488(7409), 70-72, 2012.

Behrenfeld, M.J. and Falkowski, P.G.: Photosynthetic rates derived from satellite-based chlorophyll concentration. Limnology and Oceanography, 42(1), 1-20, 1997a.

Behrenfeld M J, Falkowski P G.: A consumer's guide to phytoplankton primary productivity models. Limnology and Oceanography, 42(7), 1479-1491, 1997b.

Behrenfeld, M.J., Boss, E., Siegel, D.A. and Shea, D.M.: Carbon-based ocean productivity and phytoplankton physiology from space. Global Biogeochemical Cycles, 19, GB1006, 2005.

Boer, G.J. and Arora, V.: Temperature and concentration feedbacks in the carbon cycle. Geophysical Research Letters, 36, L02704, 2009.

Bopp, L., Aumont, O., Cadule, P., Alvain, S. and Gehlen, M.: Response of diatoms distribution to global warming and potential implications: A global model study. Geophysical Research Letters, 32, L19606, 2005.

Bopp, L., Resplandy, L., Orr, J.C., Doney, S.C., Dunne, J.P., Gehlen, M., Halloran, P., Heinze, C., Ilyina, T., Seferian, R. and Tjiputra, J.: Multiple stressors of ocean ecosystems in the 21st century: projections with CMIP5 models. Biogeosciences, 10, 6225-6245, 2013.

Bretherton, F. P.: Earth system science and remote sensing, P. IEEE, 73, 1118–1127, 1985.

Cao, J., Wang, B., Xiang, B., Li, J., Wu, T., Fu, X., Wu, L. and Min, J.: Major modes of short-term climate variability in the newly developed NUIST Earth System Model (NESM). Advances in Atmospheric Sciences, 32(5), 585-600, 2015.

Cao, J., Wang, B., Yang, Y.-M., Ma, L., Li, J., Sun, B., Bao, Y., He, J., and Zhou, X.: The NUIST Earth System Model (NESM) version 3: Description and preliminary evaluation, Geosci. Model Dev. Discuss. 2018. https://doi.org/10.5194/gmd-2017-206.

Capotondi, A., Alexander, M.A., Bond, N.A., Curchitser, E.N. and Scott, J.D.: Enhanced upper ocean stratification with climate change in the CMIP3 models. Journal of Geophysical Research: Oceans, 117(C4), 2012.

Ciais, P., C. Sabine, G. Bala, L. Bopp, V. Brovkin, J. Canadell, A. Chhabra, R. DeFries, J. Galloway, M. Heimann, C. Jones, C. Le Quéré, R.B. Myneni, S. Piao and P. Thornton.: Carbon and Other Biogeochemical Cycles. In: Climate Change

2013: The Physical Science Basis. Contribution of Working Group I to the Fifth Assessment Report of the Intergovernmental Panel on Climate Change [Stocker, T.F., D. Qin, G.-K. Plattner, M. Tignor, S.K. Allen, J. Boschung, A. Nauels, Y. Xia, V. Bex and P.M. Midgley (eds.)]. Cambridge University Press, Cambridge, United Kingdom and New York, NY, USA, 2013.

Collins, M., and Coauthors.: Long-term Climate Change: Projections, Commitments and Irreversibility. In: Climate Change 2013: The Physical Science Basis. Contribution of Working Group I to the Fifth Assessment Report of the Intergovernmental Panel on Climate Change. Stocker, T.F., D. Qin, G.-K. Plattner, et al., Eds., Cambridge University Press, Cambridge, United Kingdom and New York, NY, USA, 2013.

Cox, P.M., Betts, R.A., Jones, C.D., Spall, S.A. and Totterdell, I.J.: Acceleration of global warming due to carbon-cycle feedbacks in a coupled climate model. Nature, 408(6809), 184-187, 2000.

Cheng, W., Chiang, J.C. and Zhang, D.: Atlantic meridional overturning circulation (AMOC) in CMIP5 models: RCP and historical simulations. Journal of Climate, 26(18), 7187-7197, 2013.

Denman, K.L., G. Brasseur, A. Chidthaisong, P. Ciais, P.M. Cox, R.E. Dickinson, D. Hauglustaine, C. Heinze, E. Holland, D. Jacob, U. Lohmann, S Ramachandran, P.L. da Silva Dias, S.C. Wofsy and X. Zhang,: Couplings Between Changes in the Climate System and Biogeochemistry. In: Climate Change 2007: The Physical Science Basis. Contribution of Working Group I to the Fourth Assessment Report of the Intergovernmental Panel on Climate Change [Solomon, S., D. Qin, M. Manning, Z. Chen, M. Marquis, K.B. Averyt, M.Tignor and H.L. Miller (eds.)]. Cambridge University Press, Cambridge, United Kingdom and New York, NY, USA, 2007.

Doney, S.C., Lindsay, K., Caldeira, K., Campin, J.M., Drange, H., Dutay, J.C., Follows, M., Gao, Y., Gnanadesikan, A., Gruber, N. and Ishida, A.: Evaluating global ocean carbon models: The importance of realistic physics. Global Biogeochemical Cycles, 18, GB3017, 2004.

Dufresne, J.L., Foujols, M.A., Denvil, S., Caubel, A., Marti, O., Aumont, O., Balkanski, Y., Bekki, S., Bellenger, H., Benshila, R. and Bony, S.: Climate change projections using the IPSL-CM5 Earth System Model: from CMIP3 to CMIP5. Climate Dynamics, 40(9-10), 2123-2165, 2013.

Dunne, J.P., Sarmiento, J.L. and Gnanadesikan, A.: A synthesis of global particle export from the surface ocean and cycling through the ocean interior and on the seafloor. Global Biogeochemical Cycles, 21, GB4006, 2007.

Dutkiewicz, S., Follows, M.J. and Parekh, P.: Interactions of the iron and phosphorus cycles: A three-dimensional model study. Global Biogeochemical Cycles, 19, GB1021, 2005.

Friedlingstein, P., Cox, P., Betts, R., Bopp, L., von Bloh, W., Brovkin, V., Cadule, P., Doney, S., Eby, M., Fung, I. and Bala, G.: Climate–carbon cycle feedback analysis: results from the C4MIP model intercomparison. Journal of Climate, 19(14), 3337-3353, 2006.

Garcia, C.A.E., Garcia, V.M.T. and McClain, C.R.: Evaluation of SeaWiFS chlorophyll algorithms in the Southwestern Atlantic and Southern Oceans. Remote Sensing of Environment, 95(1), 125-137, 2005.

Garcia, H., Locarnini, R., Boyer, T., Antonov, J., Zweng, M., Baranova, O. and Johnson, D.: World Ocean Atlas 2009, vol. 4,

Nutrients (Phosphate, Nitrate, Silicate), edited by: Levitus, S. NOAA Atlas NESDIS, US Gov. Printing Office, Wash., DC, 2010.

Gregory, J.M., Dixon, K.W., Stouffer, R.J., Weaver, A.J., Driesschaert, E., Eby, M., Fichefet, T., Hasumi, H., Hu, A., Jungclaus, J.H. and Kamenkovich, I.V.: A model intercomparison of changes in the Atlantic thermohaline circulation in response to increasing atmospheric CO_2 concentration. Geophysical Research Letters, 32, L12703, 2005.

Gregory, J.M., Jones, C.D., Cadule, P. and Friedlingstein, P.: Quantifying carbon cycle feedbacks. Journal of Climate, 22(19), 5232-5250, 2009.

Griffies, Stephen M., and Coauthors.: Impacts on ocean heat from transient mesoscale eddies in a hierarchy of climate models. Journal of Climate 28(3), 952-977, 2015.

Held, I.M., Winton, M., Takahashi, K., Delworth, T., Zeng, F. and Vallis, G.K.: Probing the fast and slow components of global warming by returning abruptly to preindustrial forcing. Journal of Climate, 23(9), 2418-2427, 2010.

Hirata, T., Hardman-Mountford, N.J., Brewin, R.J.W., Aiken, J., Barlow, R., Suzuki, K., Isada, T., Howell, E., Hashioka, T., Noguchi-Aita, M. and Yamanaka, Y.: Synoptic relationships between surface Chlorophyll-a and diagnostic pigments specific to phytoplankton functional types. Biogeosciences, 8(2), 311-327, 2011.

Hood, R.R., Kohler, K.E., McCreary, J.P. and Smith, S.L.: A four-dimensional validation of a coupled physical–biological model of the Arabian Sea. Deep Sea Research Part II: Topical Studies in Oceanography, 50(22-26), 2917-2945, 2003.

Hunke, E.C., Lipscomb, W.H., Turner, A.K., Jeffery, N. and Elliott, S.: CICE: the Los Alamos Sea Ice Model Documentation and Software User's Manual Version 4.1 LA-CC-06-012. T-3 Fluid Dynamics Group, Los Alamos National Laboratory, Los Alamos N.M, 2010.

Jin, F.F.: Tropical ocean-atmosphere interaction, the Pacific cold tongue, and the El Niño-Southern Oscillation. Science, 274(5284), 76-78, 1996.

Jones, C., Robertson, E., Arora, V., Friedlingstein, P., Shevliakova, E., Bopp, L., Brovkin, V., Hajima, T., Kato, E., Kawamiya, M. Liddicoat, S., Lindsay, K., Reick, C. H., Roelandt, C., Segschneider, J., and Tjiputra, J.: Twenty-first-century compatible CO_2 emissions and airborne fraction simulated by CMIP5 earth system models under four representative concentration pathways. Journal of Climate, 26(13), 4398-4413, 2013.

Joos, F. and Spahni, R.: Rates of change in natural and anthropogenic radiative forcing over the past 20,000 years. Proceedings of the National Academy of Sciences, 105(5), 1425-1430, 2008.

Kahru, M. and Mitchell, B.G.: Blending of ocean colour algorithms applied to the Southern Ocean. Remote Sensing Letters, 1(2), 119-124, 2010.

Key, R.M., and Coauthors.: A global ocean carbon climatology: Results from Global Data Analysis Project (GLODAP). Global Biogeochemical Cycles, 18(4), 357-370, 2004.

Knutti, R. and Sedláček, J.: Robustness and uncertainties in the new CMIP5 climate model projections. Nature Climate Change, 3(4), 369-373, 2013.

Koné, V., Aumont, O., Lévy, M. and Resplandy, L.: Physical and biogeochemical controls of the phytoplankton seasonal

cycle in the Indian Ocean: A modeling study. Indian Ocean Biogeochemical Processes and Ecological Variability, 185, 147-166, 2009.

Körtzinger, A., Hedges, J.I. and Quay, P.D.: Redfield ratios revisited: Removing the biasing effect of anthropogenic CO_2. Limnology and Oceanography, 46(4), 964-970, 2001.

Larson, J., Jacob, R. and Ong, E.: The model coupling toolkit: a new Fortran90 toolkit for building multiphysics parallel coupled models. The International Journal of High Performance Computing Applications, 19(3), 277-292, 2005.

Le Quéré, C., and Coauthors.: Global carbon budget 2017. Earth System Science Data Discussions, 1-79, 2017.

Lee, C.M., Jones, B.H., Brink, K.H. and Fischer, A.S.: The upper-ocean response to monsoonal forcing in the Arabian Sea: seasonal and spatial variability. Deep Sea Research Part II: Topical Studies in Oceanography, 47(7-8), 1177-1226, 2000.

Lengaigne, M., Madec, G., Bopp, L., Menkes, C., Aumont, O. and Cadule, P.: Bio-physical feedbacks in the Arctic Ocean using an Earth system model. Geophysical Research Letters, 36, L21602, 2009.

Levin, I. and Hesshaimer, V.: Radiocarbon–a unique tracer of global carbon cycle dynamics. Radiocarbon, 42(1), 69-80, 2000.

Levitus, S., Antonov, J.I., Boyer, T.P. and Stephens, C.: Warming of the world ocean. Science, 287(5461), 2225-2229, 2000.

Lévy, M., Estublier, A. and Madec, G.: Choice of an advection scheme for biogeochemical models. Geophysical Research Letters, 28(19), 3725-3728, 2001a.

Lévy, M., Klein, P. and Treguier, A.M.: Impact of sub-mesoscale physics on production and subduction of phytoplankton in an oligotrophic regime. Journal of Marine Research, 59(4), 535-565, 2001b.

Li, G. and Xie, S.P.: Tropical biases in CMIP5 multimodel ensemble: The excessive equatorial Pacific cold tongue and double ITCZ problems. Journal of Climate, 27(4), 1765-1780, 2014.

Li, J., Wang, B. and Yang, Y.M.: Retrospective seasonal prediction of summer monsoon rainfall over West Central and Peninsular India in the past 142 years. Climate Dynamics, 48(7-8), 2581-2596, 2017.

Lin, H., Kuzminov, F.I., Park, J., Lee, S., Falkowski, P.G. and Gorbunov, M.Y.: The fate of photons absorbed by phytoplankton in the global ocean. Science, p.aab2213, 2016.

Longhurst, A., Sathyendranath, S., Platt, T. and Caverhill, C.: An estimate of global primary production in the ocean from satellite radiometer data. Journal of Plankton Research, 17(6), 1245-1271, 1995.

Luo, Y., Liu, Q. and Rothstein, L.M.: Simulated response of North Pacific Mode Waters to global warming. Geophysical Research Letters, 36(23), 2009.

Madec, G., and the NEMO team: NEMO ocean engine. Note du pôle de modélisation, No. 27, Institut Pierre-Simon Laplace (IPSL), France, 2012.

Matsumoto, K.: Radiocarbon-based circulation age of the world oceans. Journal of Geophysical Research: Oceans, 112, C09004, 2007.

McGillicuddy Jr, and Coauthors.: Influence of mesoscale eddies on new production in the Sargasso Sea. Nature, 394(6690), 263-266, 1998.

Morel, A. and Berthon, J.F.: Surface pigments, algal biomass profiles, and potential production of the euphotic layer: Relationships reinvestigated in view of remote-sensing applications. Limnology and Oceanography, 34(8), 1545-1562, 1989.

Moss, R.H., and Coauthors.: The next generation of scenarios for climate change research and assessment. Nature, 463(7282), 747-756, 2010.

Najjar, R.G.: Marine biogeochemistry, in Climate System Modeling, edited by K.E. Trenberth. Cambridge Univ. Press, New York, 1992.

NOAA ESRL Global Monitoring Division.: Atmospheric Carbon Dioxide Dry Air Mole Fractions from quasi-continuous measurements at Mauna Loa, Hawaii. Compiled by K.W. Thoning, D.R. Kitzis, and A. Crotwell. National Oceanic and Atmospheric Administration (NOAA), Earth System Research Laboratory (ESRL), Global Monitoring Division (GMD): Boulder, Colorado, USA. Version 2017-8, 2016, http://dx.doi.org/10.7289/V54X55RG.

Oschlies, A. and Garçon, V.: Eddy-induced enhancement of primary production in a model of the North Atlantic Ocean, Nature, 394, 266–269, 1998.

Polovina, J.J., Howell, E.A. and Abecassis, M.: Ocean's least productive waters are expanding. Geophysical Research Letters, 35, L03618, 2008.

Pierce, D.W., and Coauthors.: The fingerprint of human-induced changes in the ocean's salinity and temperature fields. Geophysical Research Letters, 39, L21704, 2012.

Resplandy, L., and Coauthors.: Controlling factors of the oxygen balance in the Arabian Sea's OMZ. Biogeosciences, 9, 5095-5109, 2012.

Rhein, M., S.R. Rintoul, S. Aoki, E. Campos, D. Chambers, R.A. Feely, S. Gulev, G.C. Johnson, S.A. Josey, A. Kostianoy, C. Mauritzen, D. Roemmich, L.D. Talley and F. Wang. : Observations: Ocean. In: Climate Change 2013: The Physical Science Basis. Contribution of Working Group I to the Fifth Assessment Report of the Intergovernmental Panel on Climate Change [Stocker, T.F., D. Qin, G.-K. Plattner, M. Tignor, S.K. Allen, J. Boschung, A. Nauels, Y. Xia, V. Bex and P.M. Midgley (eds.)]. Cambridge University Press, Cambridge, United Kingdom and New York, NY, USA, 2013.

Roeckner, E., and Coauthors.: The atmospheric general circulation model ECHAM 5. PART I: Model description. Rep. No. 349, Max-Planck-Institut fur Meteorologie, Hamburg, Germany, 2003.

Roesch, A., Wild, M., Gilgen, H. and Ohmura, A.: A new snow cover fraction parameterization for the ECHAM4 GCM. Clim. Dyn., 17, 933–946, 2001.

Sabine, C.L., and Coauthors.: The oceanic sink for anthropogenic CO_2. Science, 305(5682), 367-371, 2004.

Sarmiento, J. L., and N. Gruber.: Ocean Biogeochemical Dynamics. Princeton University Press, Princeton, NJ, USA, 2006.

Schneider, B., Bopp, L., Gehlen, M., Segschneider, J., Frölicher, T.L., Cadule, P., Friedlingstein, P., Doney, S.C., Behrenfeld, M.J. and Joos, F.: Climate-induced interannual variability of marine primary and export production in three global coupled climate carbon cycle models. Biogeosciences, 5(2), 597-614, 2008.

Schulz, J.-P., Dumenil, L. and Polcher, J.: On the land surface-atmosphere coupling and its impact in a single-column

atmospheric model. J. Appl. Meteorol., 40, 642–663, 2001.

Schwinger, J., and Coauthors.: Nonlinearity of ocean carbon cycle feedbacks in CMIP5 Earth system models. Journal of Climate, 27(11), 3869-3888, 2014.

Séférian, R., and Coauthors.: Skill assessment of three earth system models with common marine biogeochemistry. Climate Dynamics, 40(9-10), 2549-2573, 2013.

Skinner, L.C., and Coauthors.: Radiocarbon constraints on the glacial ocean circulation and its impact on atmospheric CO_2. Nature Communications, 8, 16010, 2017.

Steinacher, M., Joos, F., Frölicher, T.L., Bopp, L., Cadule, P., Cocco, V., Doney, S.C., Gehlen, M., Lindsay, K., Moore, J.K. and Schneider, B.: Projected 21st century decrease in marine productivity: a multi-model analysis. Biogeosciences, 7(3), 979-1005, 2010.

Stocker, T.F. and Wright, D.G.: Rapid changes in ocean circulation and atmospheric radiocarbon. Paleoceanography, 11(6), 773-795, 1996.

Takahashi, T., Broecker, W.S. and Langer, S.: Redfield ratio based on chemical data from isopycnal surfaces. Journal of Geophysical Research: Oceans, 90(C4), 6907-6924, 1985.

Takahashi, T., and Coauthors.: Climatological mean and decadal change in surface ocean pCO_2, and net sea–air CO_2 flux over the global oceans. Deep Sea Research Part II: Topical Studies in Oceanography, 56(8-10), 554-577, 2009.

Taylor, K.E.: Summarizing multiple aspects of model performance in a single diagram. Journal of Geophysical Research: Atmospheres, 106(D7), 7183-7192, 2001.

Taylor, K.E., Stouffer, R.J. and Meehl, G.A.: An overview of CMIP5 and the experiment design. Bulletin of the American Meteorological Society, 93(4), 485-498, 2012.

Teng, H., Masutani, S.M., Kinoshita, C.M. and Nihous, G.C.: Solubility of CO_2 in the ocean and its effect on CO_2 dissolution. Energy Conversion and Management, 37(6-8), 1029-1038, 1996.

Uitz, J., Claustre, H., Gentili, B. and Stramski, D.: Phytoplankton class-specific primary production in the world's oceans: seasonal and interannual variability from satellite observations. Global Biogeochemical Cycles, 24, GB3016, 2010.

Wanninkhof, R.: Relationship between wind speed and gas exchange over the ocean. Journal of Geophysical Research: Oceans, 97(C5), 7373-7382, 1992.

Wanninkhof, R., and Coauthors.: Global ocean carbon uptake: magnitude, variability and trends. Biogeosciences, 10, 1983-2000, 2013.

Wanninkhof, R., and Triñanes J.: The impact of changing wind speeds on gas transfer and its effect on global air-sea CO_2 fluxes. Global Biogeochemical Cycles, 31, 961–974, 2017.

Weaver, A. J., and Coauthors.: Stability of the Atlantic meridional overturning circulation: A model intercomparison. Geophysical Research Letters, 39, L20709, 2012.

Whitney F A.: Nutrient variability in the mixed layer of the subarctic Pacific Ocean, 1987–2010. Journal of Oceanography, 67(4), 481-492, 2011.

Yi, C., Gong, P., Xu, M. and Qi, Y.: The effects of buffer and temperature feedback on the oceanic uptake of CO2. Geophysical Research Letters, 28(5), 751-754, 2001.

Yool, A. and Popova, E.E.: Medusa-1.0: a new intermediate complexity plankton ecosystem model for the global domain. Geoscientific Model Development, 4(2), 381-417, 2011.

Zalesak, S.T.: Fully multidimensional flux-corrected transport algorithms for fluids. Journal of Computational Physics, 31(3), 335-362, 1979.

Zickfeld, K., Eby, M. and Weaver, A.J.: Carbon-cycle feedbacks of changes in the Atlantic meridional overturning circulation under future atmospheric CO_2. Global Biogeochemical Cycles, 22, GB3024, 2008.

Zickfeld, K., Eby, M., Matthews, H.D., Schmittner, A. and Weaver, A.J.: Nonlinearity of carbon cycle feedbacks. Journal of Climate, 24(16), 4255-4275, 2011.

Appendix A.

In this study, we compare the NUIST-CSM-2.0.1 simulated ocean biogeochemical fields, including nutrients, chlorophyll, marine net primary production (NPP), sea-air CO_2 flux, and ocean inventory of anthropogenic CO_2 with available observations and data-based estimates.

Data of global ocean distributions of macro-nutrients concentrations, including nitrate, phosphate and silicate are from the *World Ocean Atlas 2009* (WOA09, Garcia, et al., 2010). Distribution of dissolved inorganic carbon (DIC) in the ocean is taken from the *Global Ocean Data Project* (Key et al., 2004; Sabine et al., 2004). Both WOA09 and GLODAP data have a horizontal resolution of 1°×1° with 33 levels, and represent the climatology in the 1990s. The distribution of observed surface ocean pCO_2 and sea-air CO_2 flux for the reference year of 2000 is taken from Takahashi et al (2009), and has a spatial resolution of 4° latitude by 5° longitude.

A data-based estimate of marine net primary production (NPP) with a horizontal resolution of 1/12°×1/12° from 1998 to 2008 is used in this study (http://www.science.oregonstate.edu/ocean.productivity/index.php). NPP is calculated based on the Vertically Generalized Production Model (VGPM) which was first proposed by Behrenfeld and Falkowski (1997a, 1997b) and is widely used to estimate global marine net primary production. The standard VGPM equation is:

$$\mathrm{NPP} = \mathrm{CHL} \times {P^B}_{opt} \times day_{length} \times (0.66125 \times \frac{par}{par + 4.1}) \times z\_eu$$

Where CHL represents chlorophyll concentration from the Sea-Viewing Wide Field-of-View Sensor from 1998 to 2008 (hereafter Seawifs, Ocean Biology Processing Group, 2014) which is also used to evaluate the model-simulated chlorophyll distribution. ${P^B}_{opt}$ is the maximum C fixation rate within a water column that is a function of sea surface temperature (SST) based on a seventh-order polynomial model (Behrenfeld and Falkowski, 1997a, 1997b). SST data used here is from the NOAA/AVHRR thermal dataset. par is the photosynthetically active radiation that can be directly accessed from the SeaWiFS dataset. day_{length} is the number of hours of day light in situ and z_{eu} is the euphotic depth calculated by the Case I model

(Morel and Berthon, 1989).

To have a direct comparison between NUIST-CSM-2.0.1 results and observations, we interpolated modeled results to the corresponding grids of observational data using the distance-weighted average remapping method, i.e. 1°×1° for nutrients and DIC, and 4°×5° for sea-air flux in year of 2000. Data-based estimates of chlorophyll and NPP are interpolated from 1/12°×1/12° grids to the 1°×1° grid, and then modeled NPP and chlorophyll is also interpolated to the 1°×1° grid.

Table 1 Description of the NUIST-CSM-2.0.1 simulation experiment types

Experiment	CO_2 seen by atmosphere radiation	CO_2 seen by ocean carbon cycle
BC	Constant pre-industrial CO_2 concentration	Prescribed time-varying CO_2 concentration
RC	Prescribed time-varying CO_2 concentration	Pre-industrial CO_2 concentration
FC	Prescribed time-varying CO_2 concentration	Prescribed time-varying CO_2 concentration

Table 2. Global ocean anthropogenic CO_2 uptake simulated by NUIST-CSM-2.0.1 during different periods compared against data-based estimate (Ciais et al., 2013) (it is noted that the pre-industrial time in this study represents the year 1800 while it represents 1750 in IPCC AR5).

	Pre-industrial-2011 Cumulative PgC	1980-1989 PgC yr^{-1}	1990-1999 PgC yr^{-1}	2000-2009 PgC yr^{-1}	2002-2011 PgC yr^{-1}
IPCC AR5	155±30	2.0±0.7	2.2±0.7	2.3±0.7	2.4±0.7
NUIST-CSM	144.4	1.7	1.9	2.3	2.3

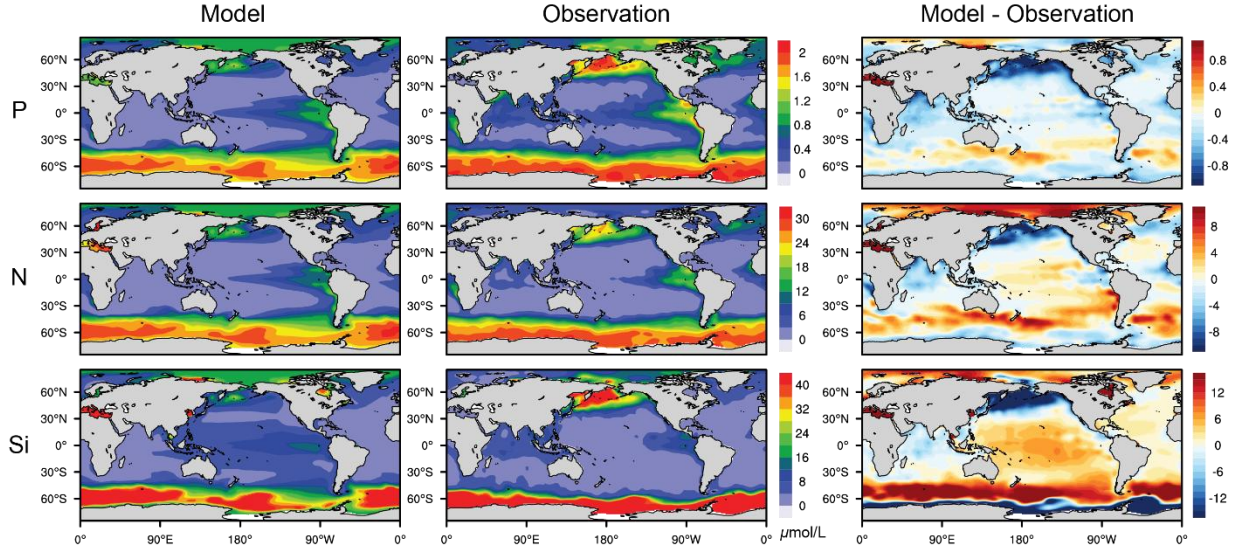

Figure 1: Annual mean upper ocean (averaged in the upper 100m) distribution of phosphate (PO_4^{3-}), nitrate (NO_3^-), and silicate (SiO_4^{2-}) averaged over the 1990s from the NUIST-CSM-2.0.1simulations (FC) and the WOA09 observation dataset.

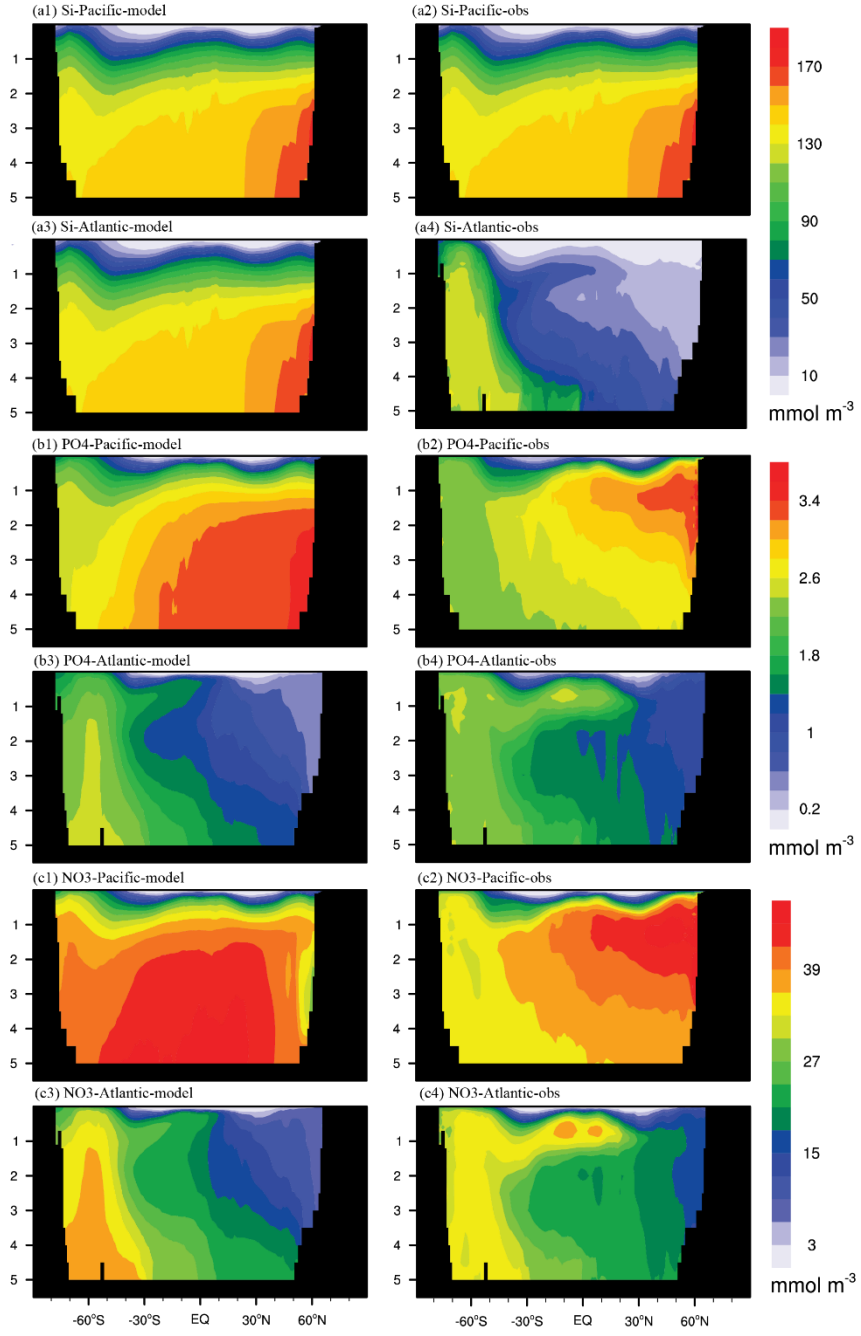

Figure 2: The latitude-depth distribution of silicate (a), phosphate (b), and nitrate (c) averaged over the 1990s (FC) compared with the WOA09 observation dataset. (with a unit of mmol m^{-3}; a1, a2, b1, b2,c1, c2 represent the distributions in the Pacific Ocean and a3, a4, b3, b4, c3, c4 represent the distributions in the Atlantic Ocean). The ocean boundary definition is derived from the WOA09 observation dataset.

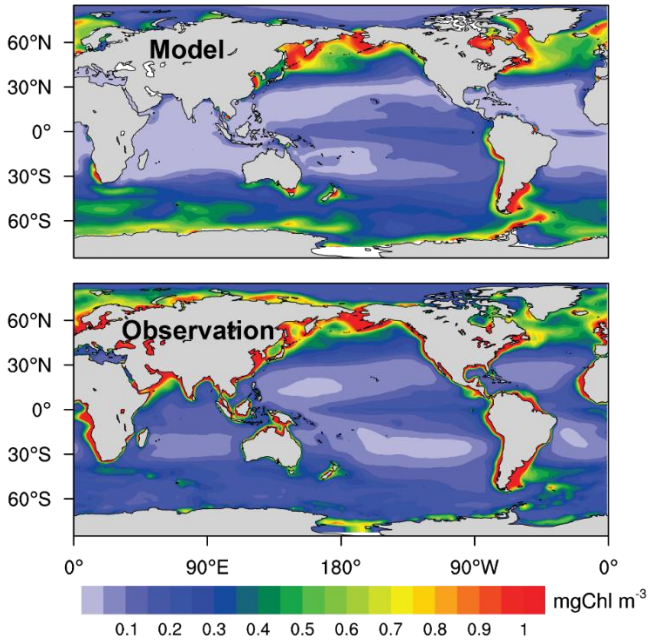

Figure 3: Annual mean surface chlorophyll concentration (mg Chl m^{-3}) averaged over the 1990s from the NUIST-CSM-2.0.1 simulations (FC) and the SeaWiFs dataset.

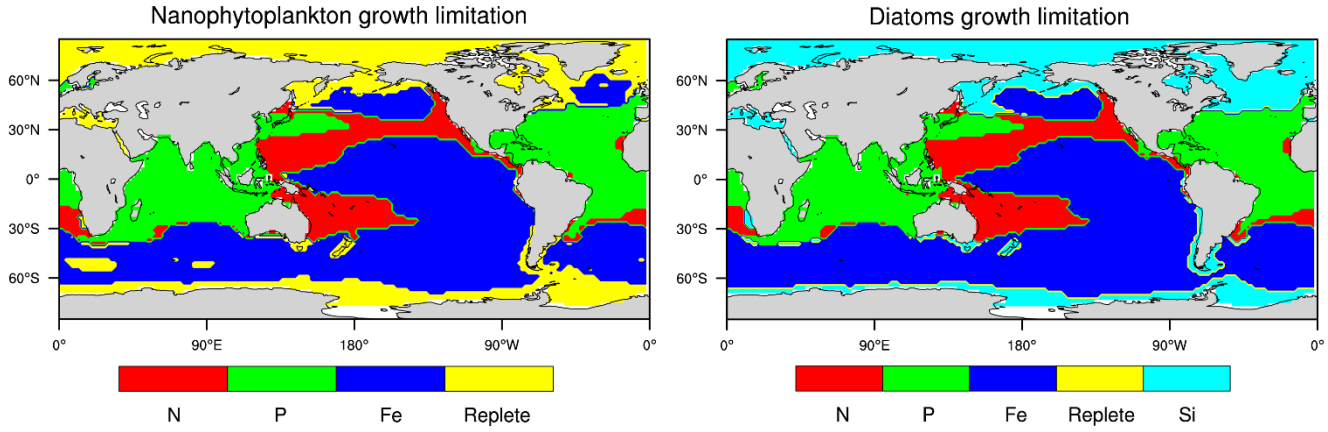

Figure 4: Diagnosed pattern of nutrients limitation over the annual time scale for nanophytoplankton and diatoms during the 1990s in the FC simulation. Shade of each color indicate the factor that most limits growth. Replete means nutrient concentrations are sufficient for the phytoplankton growth (growth rate is greater than 90% of their maximal growth rate)

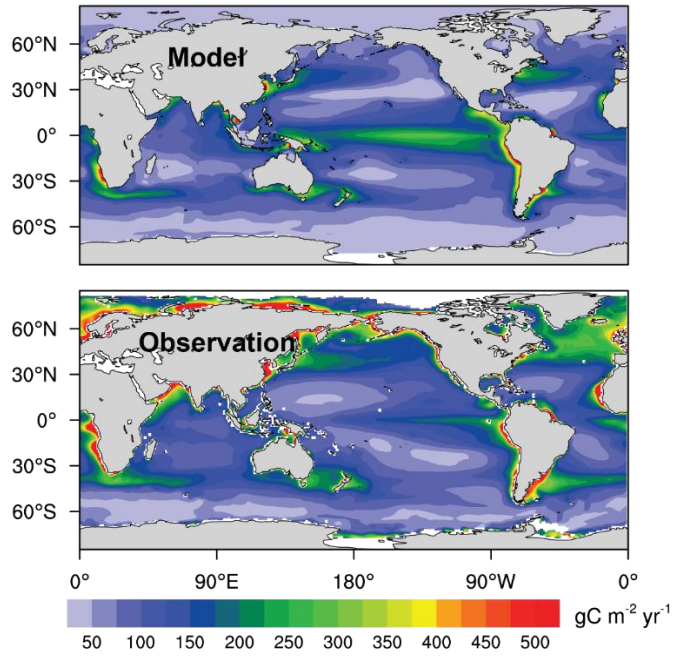

Figure 5: Annual mean distribution of vertically integrated net primary production (g C m^{-2} yr^{-1}) averaged over the 1990s from the NUIST-CSM-2.0.1simulations (FC) and observation-based estimates.

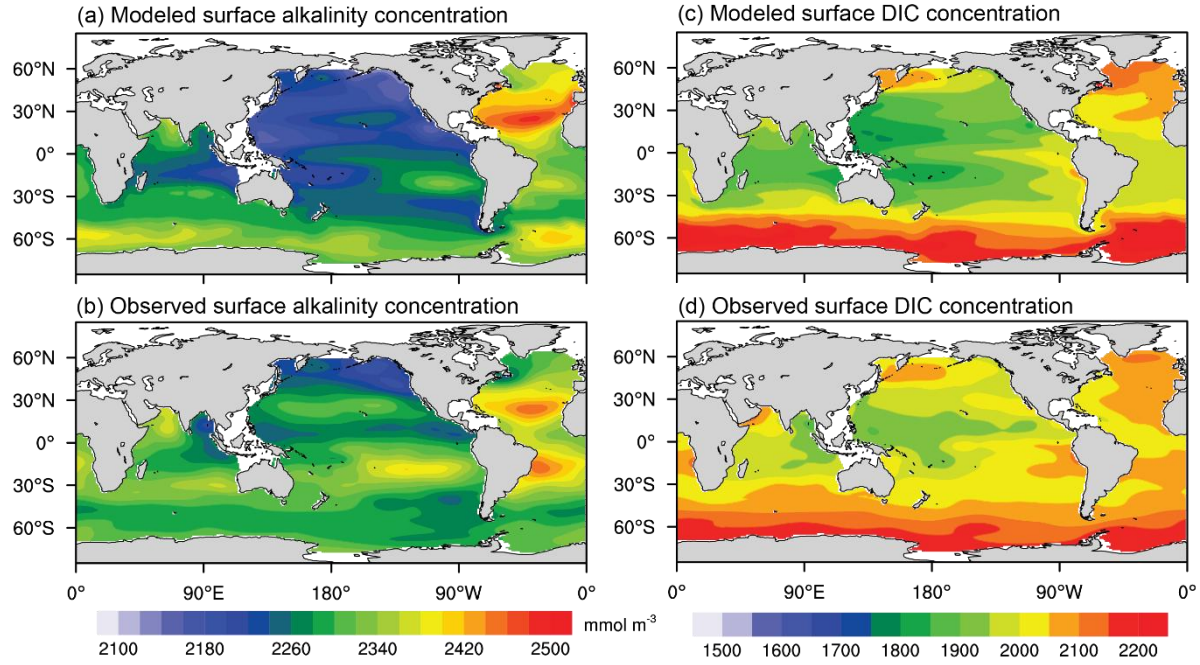

Figure 6: Annual mean distributions of upper ocean mean (0-100m) alkalinity (mmol m^{-3}) (a, b) and DIC (mol m^{-3}) (c, d) averaged over the 1990s from the NUIST-CSM-2.0.1simulations (FC) (a, c) and data-based estimates (b, d).

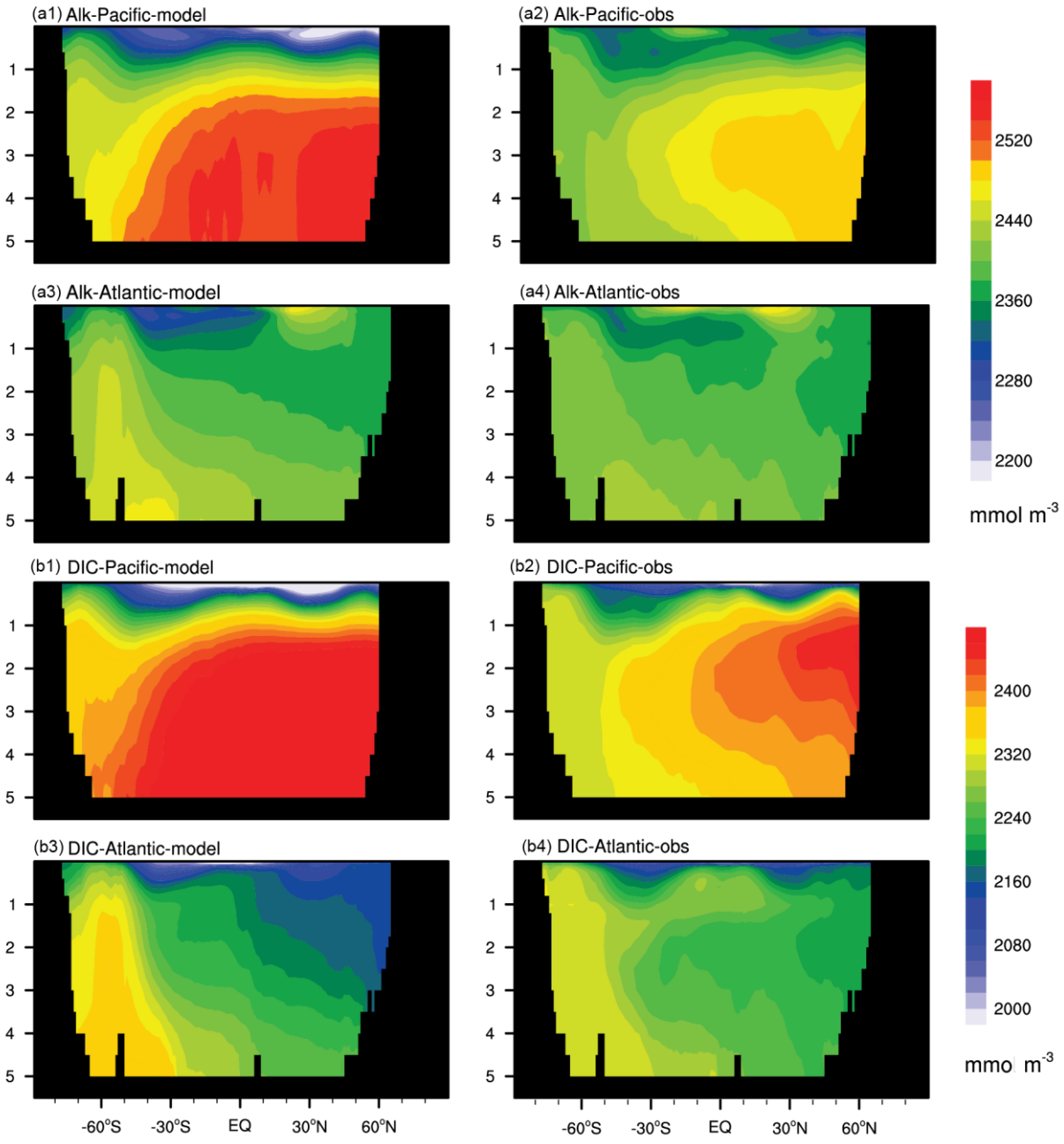

Figure 7: The latitude-depth distributions of the alkalinity (a) and DIC (b) averaged over 1990s (FC) compared with WOA09 observations (with a unit of mmol m^{-3}; a1, a2, b1, b2 represent the distributions in the Pacific Ocean and a3, a4, b3, b4 represent the distributions in the Atlantic Ocean). The ocean boundary definition is derived from the WOA09 observation dataset.

5

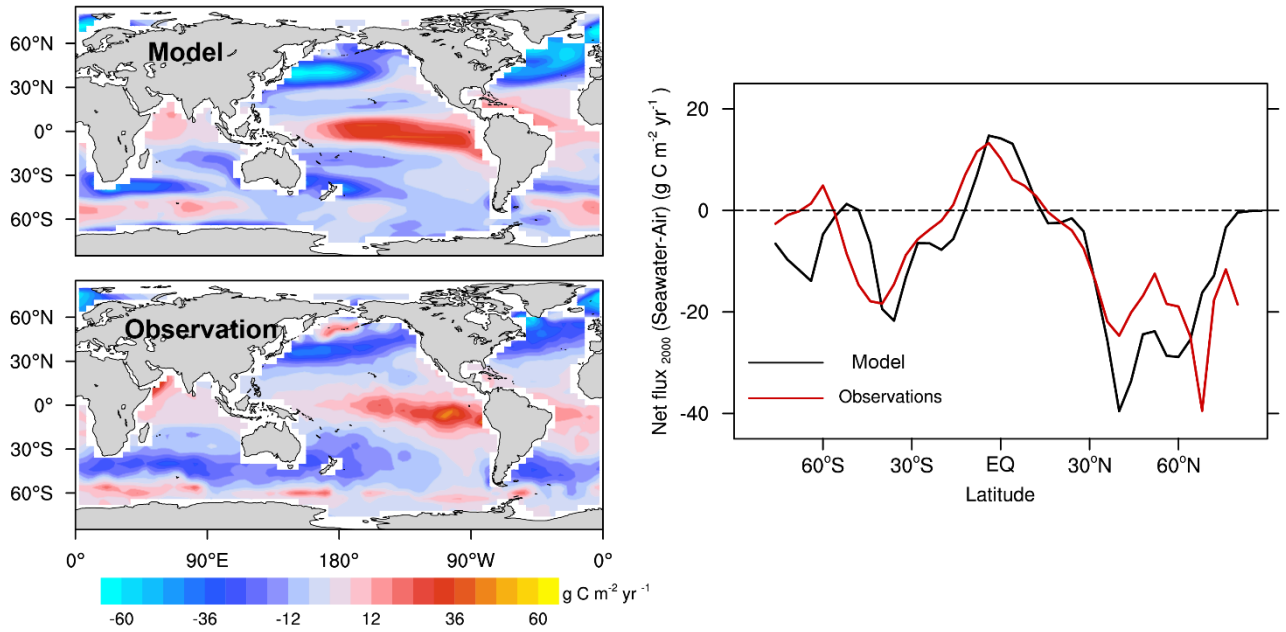

Figure 8: NUIST-CSM-2.0.1 simulated (FC run) sea-air CO_2 flux (g C m^{-2} yr^{-1}) at year 2000 against observational data. Left panels are geographical distributions and right panel is zonal mean pattern. Positive values represent CO_2 flux out of the ocean, and negative values represent CO_2 flux into the ocean

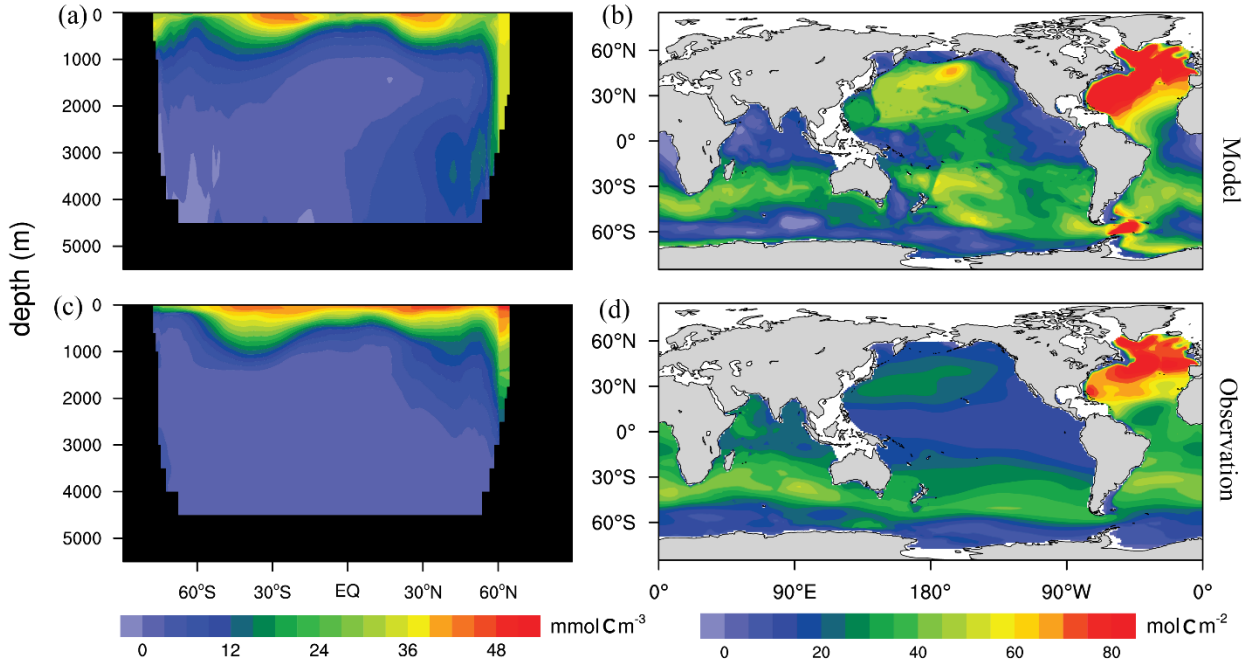

Figure 9: Latitude-depth distribution of anthropogenic DIC (mmol C m^{-3}) from the FC simulation (a) and data-based estimates (c). Vertically integrated column inventory of anthropogenic DIC (mol C m^{-2}) from the FC simulation (b) and data-based estimates (d)

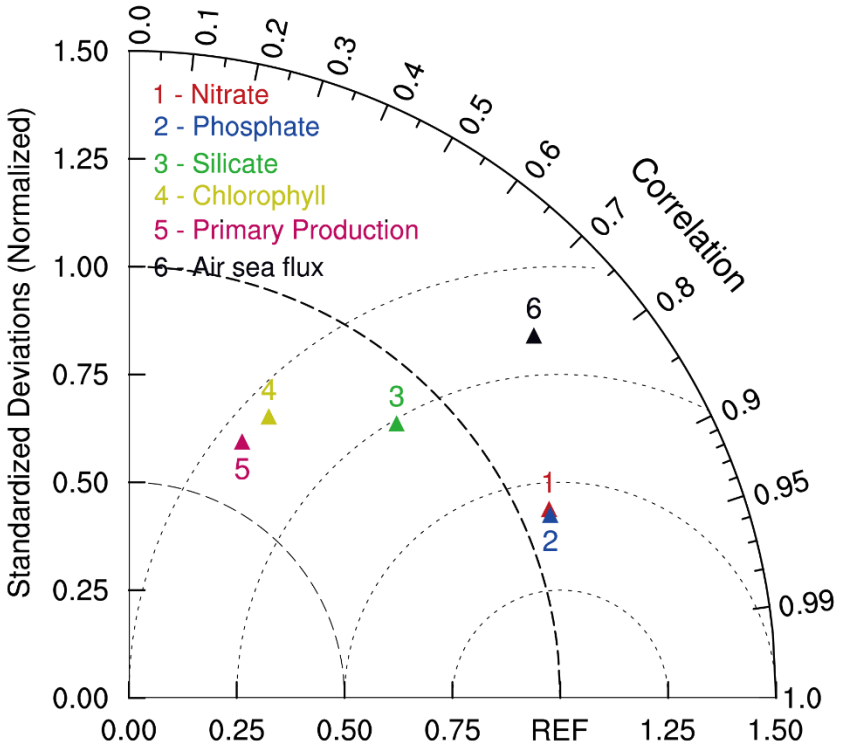

Figure 10: Taylor diagram comparing statistical patterns of annual mean carbon-related fields between the NUIST-CSM-2.0.1 simulation (FC) and corresponding observations, including upper ocean nitrate, phosphate, silicate, alkalinity, chlorophyll concentration, vertically-integrated net primary production, and sea-air CO_2 flux. All fields are normalized by the standard deviation of corresponding observations. Thus, observation fields have a standard deviation of one, which is represented by REF. The distance between the model points and the reference point indicate the root-mean-square (RMS) difference between model simulation and observations.

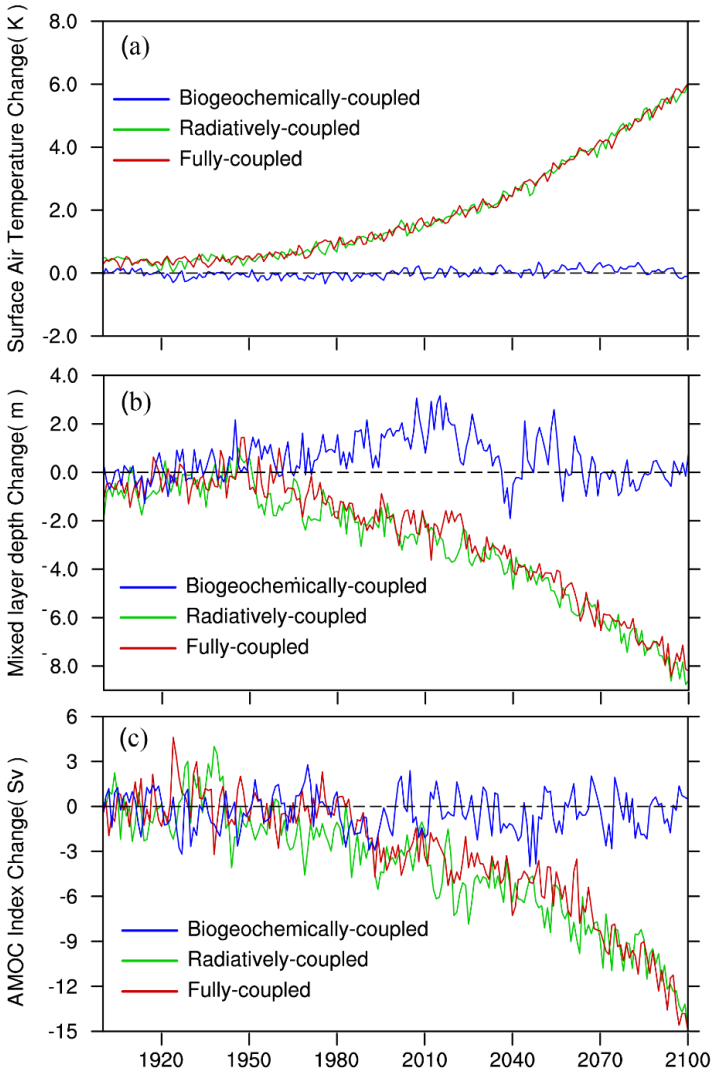

Figure 11: Time series of climate changes (relative to pre-industrial) from 1900 to 2100 for the simulation of fully-coupled, biogeochemically-coupled, and radiatively-coupled simulations. (a) global and annual mean surface air temperature, (b) global and annual mean mixed layer depth (the depth where the difference in potential density is 0.01 kg m^{-3} relative to the sea surface) and (c) Atlantic meridional overturning circulation index (maximum zonal mean stream function of the Atlantic Ocean at 30°N).

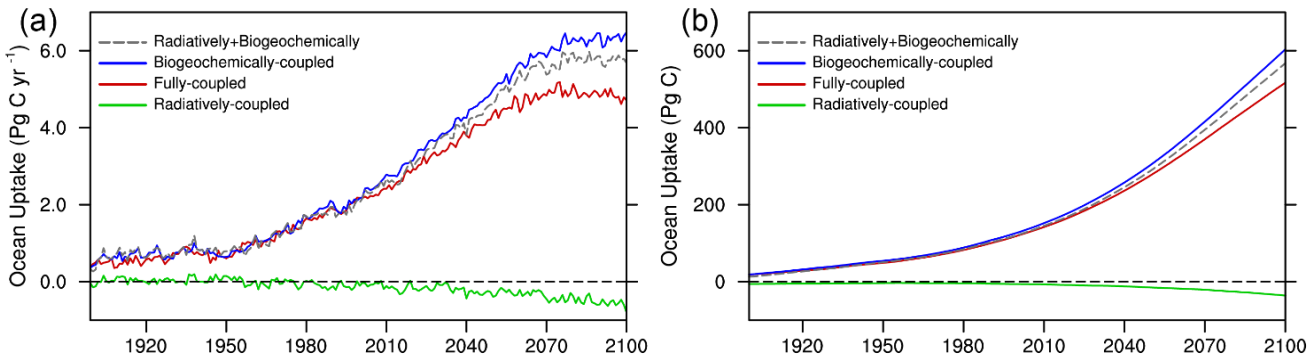

Figure 12. The NUIST-CSM-2.0.1 simulated (a) annual mean oceanic CO_2 uptake and (b) cumulative oceanic CO_2 uptake for the simulation RC, BC,FC, and the linear sum of BC and RC from 1900 to 2100.

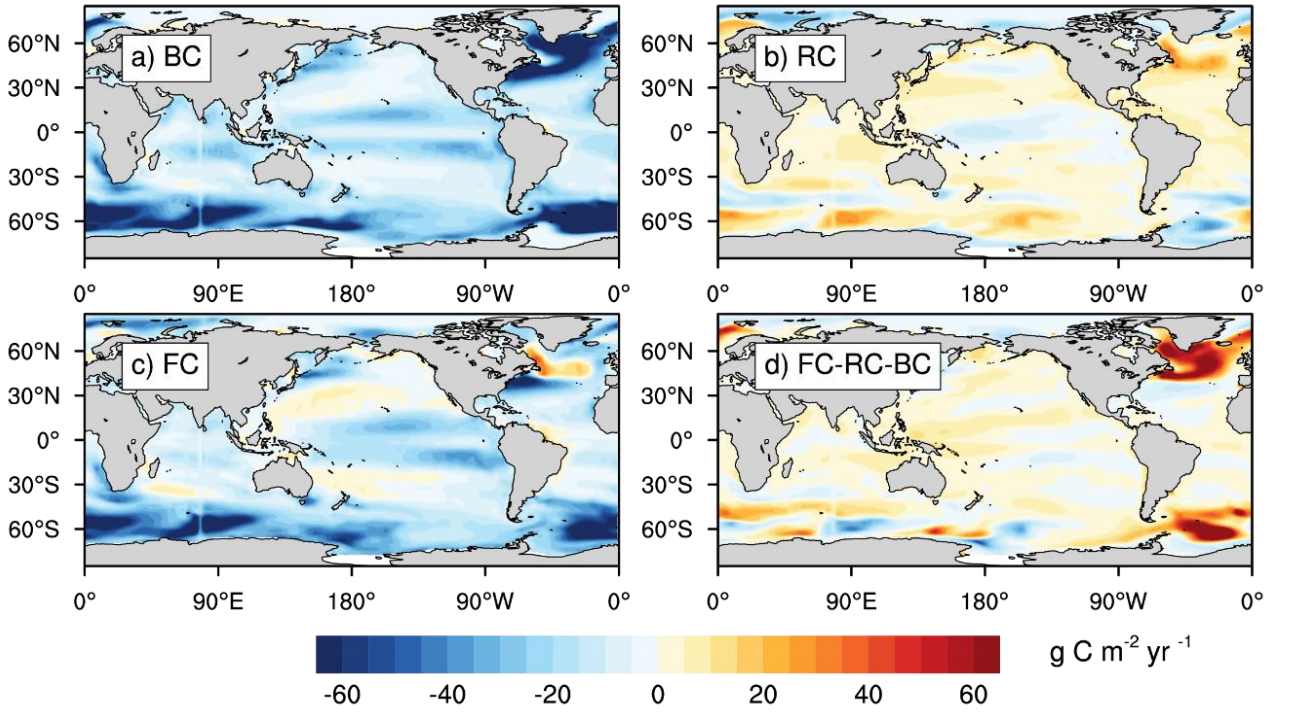

Figure 13. Spatial distribution of anthropogenic sea-air CO_2 flux at the end of the 21st century (mean of 2091-2100) from the (a) BC, (b) RC, and (c) FC, respectively. Also shown is the difference between FC simulation and the sum of RC and BC simulations (FC-RC-BC). Positive values represent CO_2 flux out of ocean, and negative values represent CO_2 flux into the ocean.

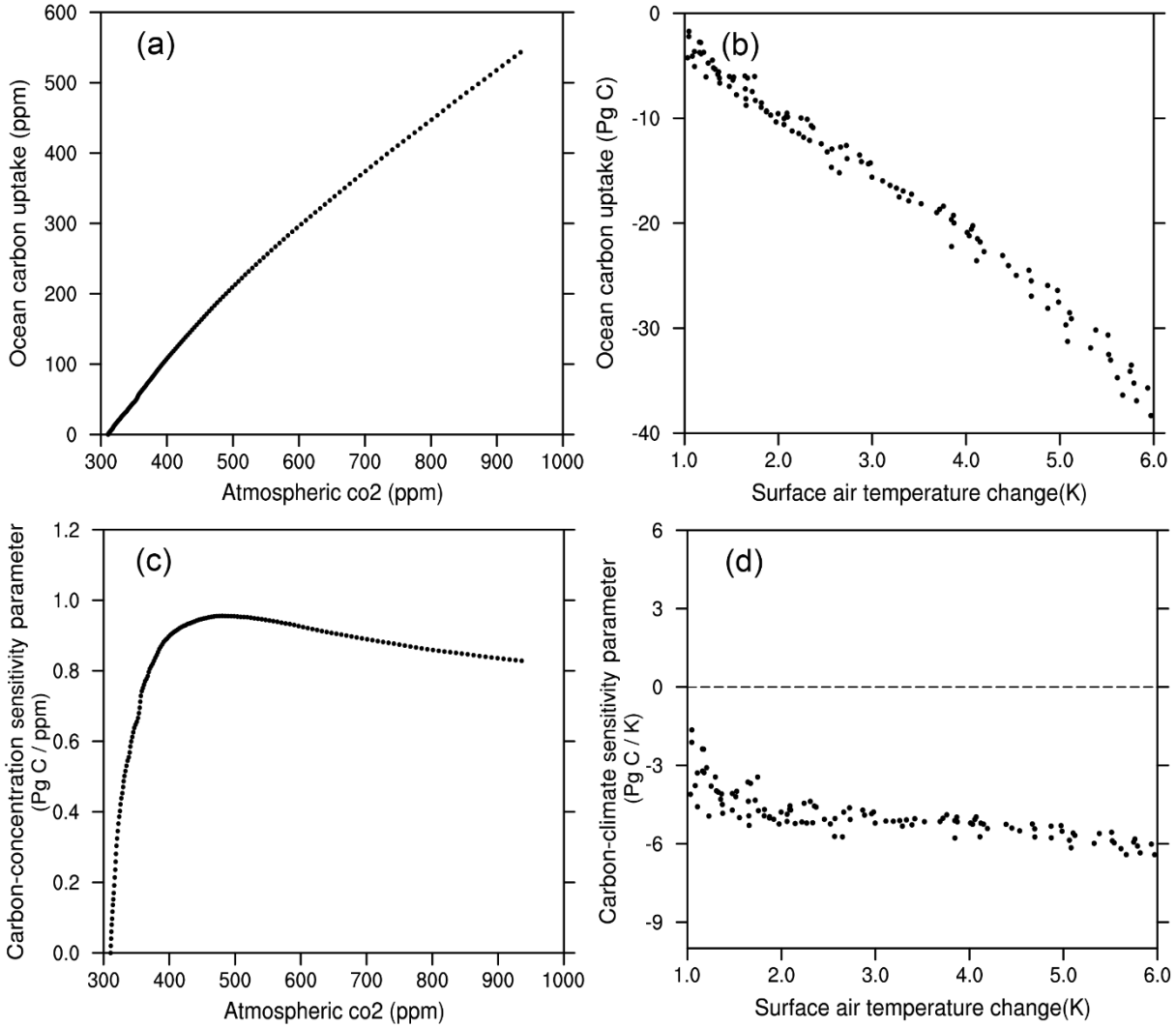

Figure 14: The cumulated ocean uptake against (a) the atmospheric CO2 in the BC experiments and (b) the global mean surface air temperature change in the RC experiments. Also shown is time evolution of diagnosed carbon-concentration sensitivity parameter as a function of atmospheric CO2 (c) and carbon-climate sensitivity parameter as a function of global mean surface air temperature change (d). Here we only diagnose the results from 1950 to 2100.

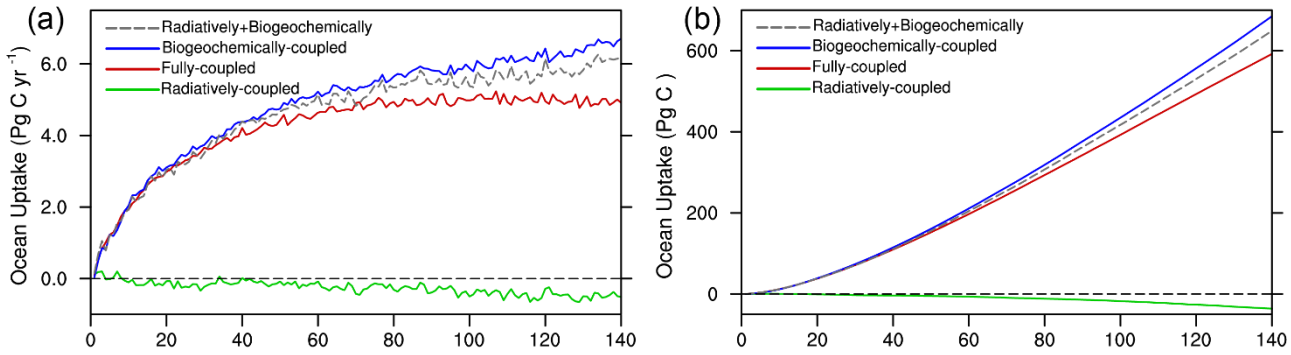

Figure 15: Same as Figure 9, but for 1% per year CO_2 increase run.

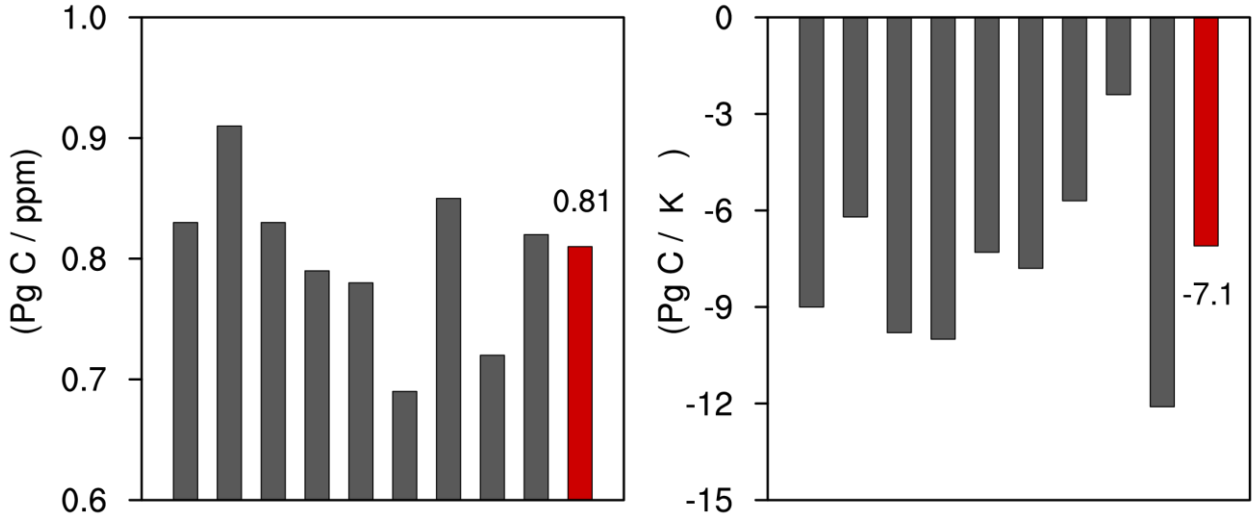

Figure 16: Carbon-concentration sensitivity parameter (left panel) and carbon-climate sensitivity parameter (right-panel) diagnosed from CMIP5 and NUIST-CSM-2.0.1 benchmark simulations with the increase of atmospheric CO_2 at a rate of 1% per year. CMIP5 model results are in grey, and NUIST-CSM-2.0.1 results are in red. CMIP5 models includes MPI-ESM-LR, IPSL-CM5A-LR, BCC-CSM1, HADGEMS, UVicESCM2.9, CaNUIST-CSM2, NorESM-ME, CESM1-BGC and MIROC ESM (from left to right).